

1
2
3 **Self-Supported Hydrous Iridium-Nickel Oxide Two-Dimensional Nanoframes**
4
5
6 **for High Activity Oxygen Evolution Electrocatalysts**
7
8
9

10
11 Fernando Godínez-Salomón,¹ Luis Albiter,¹ Shaun M. Alia,² Bryan S. Pivovar,² Luis E.
12
13 Camacho-Forero,³ Perla B. Balbuena,³ Rubén Mendoza-Cruz,⁴ Maria Josefina Arellano-
14
15 Jimenez,⁴ and Christopher P. Rhodes^{1,*}
16
17
18
19

20 ¹ *Department of Chemistry and Biochemistry, Texas State University*

21
22 *San Marcos Texas 78666, USA*
23

24 ² *Chemistry and Nanoscience Center, National Renewable Energy Laboratory, Golden,*

25
26
27 *Colorado 80401, USA*
28
29

30 ³ *Department of Chemical Engineering, Texas A&M University, College Station, Texas 77843,*

31
32 *USA*
33
34

35 ⁴ *Department of Physics and Astronomy, University of Texas at San Antonio,*

36
37
38 *San Antonio, Texas 78249, USA*
39
40
41
42

43 * Corresponding author: Tel.: 512.245.6721, Fax: 512.245.2374, e-mail address:

44
45
46 cprhodes@txstate.edu
47
48
49
50
51
52
53
54
55
56
57
58
59
60

Abstract

Oxygen evolution reaction (OER) electrocatalysts with high activity, high stability, and low costs are needed for proton-exchange membrane (PEM) electrolyzers. Based on the high cost and limited supply of iridium, approaches that result in iridium-based OER catalysts with increased catalytic activity are of significant interest. We report a carbon-free, self-supported hydrous iridium-nickel oxide two-dimensional nanoframe structure synthesized by thermal treatment of iridium-decorated nickel oxide nanosheets under reducing conditions and subsequent chemical leaching in acid. The catalyst nanoarchitecture contains an interconnected network of metallic iridium-nickel alloy domains with hydrous iridium oxide and nickel oxide located in the surface region. The electrochemical oxidation step maintains the three-dimensional nanoarchitecture and results in a thin (~ 5 Å) oxide/hydroxide surface layer. The temperature used for thermal reduction was found to strongly affect the catalyst surface structure and OER activity. Utilizing a lower thermal reduction temperature of 200 °C was determined to provide a higher relative surface concentration of hydroxides and nickel oxide and result in higher OER activities compared with materials treated at 300 °C. The 200 °C-treated hydrous iridium-nickel oxide electrocatalyst showed 15 times higher initial OER mass activity than commercial IrO₂, and the activity remained 10 times higher than IrO₂ after accelerated durability testing. Density functional theory (DFT) calculations and analysis of the experimental Tafel slopes support that the second electron transfer step is the rate-limiting step for the reaction. The DFT calculations demonstrate that Ni substitution on the IrO₂ surface lowers the activation energy for adsorbed intermediates of the second electron transfer step of the OER reaction. This work establishes that noble metal-decorated metal oxide nanosheets can be transformed into high surface area, carbon-free electrocatalyst nanostructures with high catalytic activities and molecular accessibility and reveals the importance of using controlled thermal reduction temperatures to alter the surface structure and OER activity.

Keywords: Two-dimensional materials, nanoframes, nanoarchitectures, electrocatalysts, oxygen evolution reaction, proton exchange membrane (PEM) electrolyzers

1. Introduction

Hydrogen has numerous uses for industrial processes, chemical synthesis, and as a fuel for fuel cells that provide clean, efficient power for automobiles, forklifts, and other applications. Currently, a significant proportion of hydrogen is made from fossil fuels. Electrochemical water splitting can produce hydrogen and oxygen from water and electricity and be powered by clean, renewable sources including wind and solar energy. Since many renewable energy sources are intermittent, water electrolyzers also provide the ability to store excess energy as hydrogen.¹

Proton exchange membrane (PEM) electrolyzers that function under acidic conditions allow high voltage efficiencies at high current densities, high pressure operation, and fast kinetics for the cathodic hydrogen evolution reaction (HER).²⁻³ In contrast to fast kinetics of the HER, the anodic oxygen evolution reaction (OER) exhibits sluggish reaction kinetics that results in high overpotentials and significant efficiency losses.^{2,4} Due to the highly oxidative potential and highly corrosive acidic conditions of PEM electrolyzers, the stability of oxygen evolution catalysts is also a significant challenge, with typical trends showing the most highly active OER catalysts also being highly unstable.¹ The development of advanced PEM OER catalysts with high activity, extended durability, and lower costs is a key challenge.^{1,5}

Although ruthenium-based catalysts (metallic Ru and RuO_x) have shown the highest activities of acidic OER catalysts, under practical operating conditions Ru-based catalysts show significant instability with substantial dissolution that leads to catalyst degradation.² Based on the instability of Ru-based catalysts, iridium-based catalysts (metallic Ir and IrO_x) have been investigated to provide acidic OER catalysts that have both high activities and reasonable

1
2
3 stabilities.^{1,6} Iridium is a platinum-group metal (PGM) with high costs and limited global supply.
4
5 Increasing the OER mass activity (A_{Ir}^{-1}) of Ir can reduce the amount of Ir required and lower the
6
7 cost of PEM electrolyzers.
8
9

10 Substitution with non-noble transition metals (e.g. Co, Ni, etc.) within IrO_2 and RuO_2 has
11
12 been investigated as an approach to develop higher activity acidic OER electrocatalysts.⁷⁻⁹ Prior
13
14 density functional theory (DFT) calculations showed that doping RuO_2 with Co or Ni within
15
16 bridging sites resulted in lower overpotentials, which was attributed to facilitating proton transfer
17
18 from M-OH or M-OOH reaction intermediates during the OER reaction.¹⁰ Doping of Co within
19
20 RuO_2 and IrO_2 was shown from DFT calculations to alter the electron density and influence
21
22 changes in the binding energies of intermediates resulting in structures with lower activation
23
24 energies.⁸ In addition to computational studies, a number of experimental studies have
25
26 investigated interacting Ni within IrO_x to increase the OER activity.^{9,11-15} In model thin films,
27
28 interaction of Ni within IrO_x was shown to yield a 20-fold improvement in Ir OER mass activity
29
30 over pure IrO_x .⁹ The effect of Ni on the activity was explained by the leaching of unstable Ni that
31
32 promoted the formation of structurally flexible and reactive OH groups that act as reactive surface
33
34 intermediates.⁹
35
36
37
38
39

40 In addition to OER electrocatalysts with high activity, obtaining high stability is needed
41
42 for PEM water electrolyzers, and OER catalyst degradation involves a number of factors including
43
44 dissolution, support corrosion, Oswald ripening, particle growth, and changes in the catalyst
45
46 surface structure.¹ Regarding Ir-Ni structures, despite the higher activity of the Ir-Ni oxide films,
47
48 Ir dissolution was ~34-47 times higher within Ir-Ni oxide films than IrO_x .⁹ Ir-Ni bimetallic
49
50 nanoparticles were shown to exhibit very high activities;¹³ however, the Ir-Ni bimetallic
51
52 nanoparticles were deposited on a carbon black support, and significant degradation occurred after
53
54
55
56
57
58
59
60

1
2
3 12 hours under constant potential testing which may result from degradation of the carbon support.
4
5 Carbon is not a viable long-term support material for OER catalysts since carbon degradation
6
7 occurs at high electrochemical potentials required for the reaction.¹⁶ Rather than using carbon
8
9 supports, IrNiO_x core-shell particles supported on antimony-doped tin oxide (ATO) were
10
11 previously shown to result in improved activities and high stabilities.¹¹ However, the activity of
12
13 ATO-supported IrNiO_x (~80 A g_{Ir}⁻¹ at 1.51 V_{RHE})¹¹ is still significantly lower than the activity of
14
15 carbon-supported Ir-Ni bimetallic nanoparticles (498 A g_{Ir}⁻¹ at 1.51 V_{RHE}).¹³ Recent work
16
17 demonstrated thin films of IrO_x/SrIrO₃ resulted in high activity and stability OER electrocatalysts
18
19 per square centimeter of oxide catalyst.¹⁷ Obtaining an electrocatalyst structure that provides both
20
21 high activity and high stability, particularly at high current densities, remains a challenge.
22
23
24
25

26 Rather than using supported structures, unsupported (self-supported) electrocatalyst
27
28 structures with three-dimensional interconnected porous networks offer the opportunity to avoid
29
30 support degradation and reduce nanoparticle aggregation,¹⁸ and therefore can potentially provide
31
32 electrocatalysts with improved stability. Recently reported iridium-nickel (Ir-Ni) and iridium-
33
34 cobalt (Ir-Co) nanowires, after acid leaching, showed improved mass activities compared with
35
36 commercial Ir nanoparticles and exhibited relatively high durabilities.⁵ We recently reported a
37
38 new class of unsupported, carbon-free metallic structures derived from controlled thermal
39
40 treatment of 2D metal hydroxides with decorated metals which we termed “two-dimensional (2D)
41
42 nanoframes” due to their hierarchical 2D framework consisting of an interconnected solid phase
43
44 and an interpenetrating pore network.¹⁹ Metallic Ni-Pt 2D nanoframes have direct interaction of
45
46 Pt with Ni which results in very high oxygen reduction reaction (ORR) specific activity, and the
47
48 integrated carbon-free network provides high stability at elevated potentials (up to 1.3 V_{RHE}).
49
50
51
52
53
54
55
56
57
58
59
60

1
2
3 Building from our study of Ni-Pt 2D nanoframe ORR catalysts, in this work we
4 investigated the synthesis, structure, OER activities, and stabilities of nickel-iridium (Ni-Ir) 2D
5 nanoframes derived from Ir-decorated NiO nanosheets. Compared with prior work that
6 investigated forming unsupported Ir-Ni structures from deposition of Ir onto metallic Ni
7 nanowires⁵ and from pyrolysis of IrCl₃ and NiCl₂ precursors,¹⁴ we explored Ir-Ni
8 nanoarchitectures obtained from thermal and chemical treatment of Ir-decorated NiO nanosheets
9 which result in a unique 3D morphology, surface structure, and high OER activity. We evaluated
10 the effects of thermal treatment temperature, acid leaching, and electrochemical oxidation on the
11 material structure and OER activity and stability. Experimental and theoretical approaches were
12 correlated in order to obtain insight into the effect of atomic surface reconstruction and
13 thermodynamic and kinetic factors involved with improving the catalytic activity of 2D
14 nanoframes for electrochemical oxygen evolution. The structure, activity and stability of a
15 commercial IrO₂ material were also evaluated to allow direct comparison with the electrochemical
16 performance of Ni-Ir 2D nanoframes. The unique architecture of Ni-Ir 2D nanoframes combines
17 local highly active catalytic sites within an interconnected network and results in 18 times higher
18 initial OER mass activity than IrO₂.

2. Results and Discussion

21
22
23
24
25
26
27
28
29
30
31
32
33
34
35
36
37
38
39
40
41
42
43
44 **Synthesis Approach.** Ni-Ir 2D nanoframes were synthesized using a sequence of steps as
45 shown in Figure 1A consisting of (i) formation of Ni(OH)₂ nanosheets using a rapid (13 min)
46 microwave-assisted process (ii) thermal treatment in air to form NiO nanosheets, (iii) deposition
47 of Ir onto the NiO nanosheets, (iv) controlled temperature/atmosphere treatments (either 200 °C or
48 300 °C) under reducing conditions (H₂/Ar, 5/95 vol %), and (v) a chemical leaching step in nitric
49 acid (0.05 M HNO₃) at 80 °C for 2 h under Ar atmosphere (details provided in Methods and ESI).

1
2
3 After depositing Ir onto the NiO nanosheets, thermal treatment under reducing conditions was
4 performed to promote Ir-Ni interaction through transforming the NiO:Ir structure into an integrated
5
6 metallic Ni-Ir phase. Our prior study showed that treating Pt-decorated Ni(OH)₂ at temperatures
7
8 of 200 °C or 300 °C under H₂/Ar resulted in Ni-Pt 2D nanoframes with different surface structures
9
10 and substantially different oxygen reduction specific activities.¹⁹ Based on this prior result, we
11
12 investigated treating NiO:Ir at different temperatures (either 200 °C or 300 °C) to determine the
13
14 effect of thermal treatment temperature on the structure and oxygen evolution activity and stability.
15
16
17 The chemical leaching step was performed to remove unstable non-noble metals (in this case Ni)
18
19 within the structure. The samples were noted as NiO (NiO nanosheets), NiO:Ir (Ir-decorated NiO
20
21 nanosheets), NiIr-200 (NiO:Ir treated at 200 °C under H₂/Ar), NiIr-300 (NiO:Ir treated at 300 °C
22
23 under H₂/Ar), NiIr-200-CL (NiIr-200 after chemical leaching), and NiIr-300-CL (NiIr-300 after
24
25 chemical leaching).
26
27
28
29
30
31
32
33
34
35
36
37
38
39
40
41
42
43
44
45
46
47
48
49
50
51
52
53
54
55
56
57
58
59
60

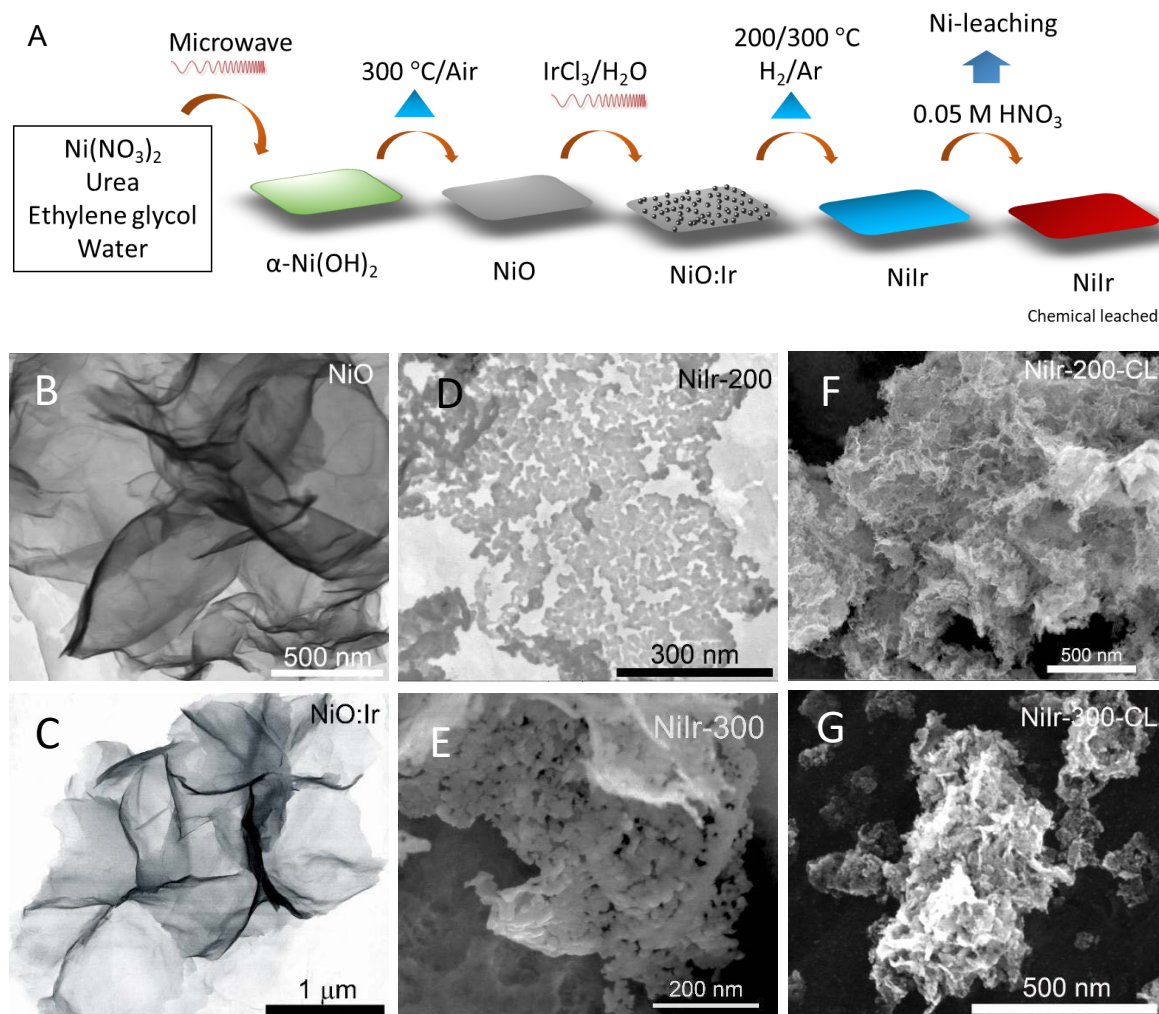


Figure 1. (A) Schematic representation of the experimental steps for the synthesis of two-dimensional (2D) Ni-Ir nanoframes; scanning electron microscopy (SEM) images the NiO nanosheet precursor (B), as-prepared NiO:Ir (C), after thermal treatment under H₂/Ar at 200 °C (NiIr-200) (D) or at 300 °C (NiIr-300) (E), and after chemical leaching in 0.05 M HNO₃ at 80 °C for 2 h, NiIr-200-CL (F) and NiIr-300-CL (G).

Analysis of the Morphologies and Elemental Compositions of Ni-Ir 2D Nanoframes and Precursor Materials. Scanning electron microscopy (SEM) was used to characterize the morphologies of the Ni-Ir 2D nanoframes and precursor materials. The SEM image of the Ni(OH)₂ nanosheets synthesized using a microwave-assisted process shows the precursor material is composed of interconnected nanosheets, and the X-ray diffraction pattern is consistent with the α -Ni(OH)₂ phase (ESI, Figure S1). After thermal treatment in air, the α -Ni(OH)₂ nanosheets were

1
2
3 transformed to a NiO phase (as supported by XRD, below) and the nanosheet morphology was
4 retained showing lateral sheet sizes of $\sim 1 \mu\text{m}$ (Figure 1B). After Ir deposition, the morphology of
5 the NiO:Ir sample (Figure 1C) remained very similar to the NiO precursor, however at higher
6 magnification surface porosity was detected which may be associated with NiO corrosion by a
7 galvanic replacement reaction with Ir species. The thermal treatment of the NiO:Ir nanosheets at
8 either 200 °C or 300° C (NiIr-200 and NiIr-300, respectively) resulted in significant structural
9 changes. The material was transformed by the thermal treatment from a nanosheet architecture
10 into a highly porous two-dimensional framework structure (Figure 1D,E). After the thermal
11 treatment, the material consists of an interconnected solid network and interpenetrating pore
12 network, as can be observed within the SEM images. The morphologies of the Ni-Ir
13 nanoarchitectures are similar to those of our previously reported Ni-Pt 2D nanoframes.¹⁹ A
14 particularly important attribute of the Ni-Ir 2D nanoframes is that the structure contains a highly
15 porous three-dimensional interconnected solid network, rather than separate particles, as can
16 clearly be observed within the SEM images. The interconnected solid network has the potential
17 to improve stability by preventing particle agglomeration, particle detachment, Oswald ripening
18 and/or carbon corrosion, which are problems commonly observed with nanoparticles supported on
19 carbonaceous materials.¹⁹⁻²¹ After the chemical leaching step, the NiIr-200-CL and NiIr-300-CL
20 samples maintain the interconnected network structure (Figure 1F,G), however as discussed
21 below, substantial structural changes due to atomic surface reconstruction and micropore
22 formation are observed.
23
24
25
26
27
28
29
30
31
32
33
34
35
36
37
38
39
40
41
42
43
44
45
46
47
48
49
50
51
52
53
54
55
56
57
58
59
60

1
2
3 High surface area and porosity are key attributes of 3D electrocatalyst structures to allow
4 significant available surface for the catalytic reaction and molecular accessibility to the
5 catalytically active site.²² In addition to high surface area, the pore structure of the nanostructured
6 catalyst is particularly important to minimize mass transport losses. The mobility of ions within
7 small pores (less than ~ 1 nm) has been shown to be orders of magnitude slower than within bulk
8 electrolyte.²²⁻²³ The presence of mesopores (pores >2 nm to 50 nm) within the 3D electrocatalyst
9 structure is highly desirable since pores within this range are accessible to the electrolyte and
10 reactants and also small enough to allow high surface areas for the catalyst.^{22,24} Nitrogen
11 physisorption measurements were used to determine the Brunauer–Emmett–Teller (BET) surface
12 areas and pore size distributions of the Ni-Ir 2D nanoframes and precursor materials (ESI, Figure
13 S5 and Table S2). After the chemical leaching step, the NiIr-200-CL and NiIr-300-CL samples
14 showed BET surface areas of 72 ± 3 and 70 ± 4 $\text{m}^2 \text{g}^{-1}$ respectively which are higher than BET
15 surface areas of some commercial IrO_2 catalysts ($35\text{-}66$ $\text{m}^2 \text{g}^{-1}$).²⁴⁻²⁵ The NiIr-200-CL and NiIr-
16 300-CL catalysts showed mean pore diameters of 22 ± 2 and 26 ± 3 nm (ESI, Table S2) which
17 supports the presence of mesopores within the catalysts, and the pore size distribution plot of NiIr-
18 200-CL shows the presence of a significant distribution of pores in the mesopore and macropore
19 (>50 nm) range (ESI, Figure S5).

20
21
22
23
24
25
26
27
28
29
30
31
32
33
34
35
36
37
38
39
40
41
42
43
44
45
46
47
48
49
50
51
52
53
54
55
56
57
58
59
60
Elemental analysis of the amount of Ir and Ni within NiIr-200-CL and NiIr-300-CL was
determined from inductively coupled plasma atomic emission spectroscopy (ICP-AES) and
showed 65.5 wt % Ir and 18.0 % Ni (atomic ratio: $\text{Ir}_1\text{Ni}_{0.90}$) for NiIr-200-CL and 63.0 wt % Ir and
18.7 wt % Ni for NiIr-300-CL (atomic ratio: $\text{Ir}_1\text{Ni}_{0.97}$), indicating a higher relative concentration
of Ni was present within NiIr-300-CL compared with NiIr-200-CL. Energy-dispersive X-ray
spectroscopy (EDS) elemental mapping analysis of the Ni-Ir 2D nanoframes and precursor

1
2
3 materials shows a uniform distribution of Ni, Ir and O within the structures (ESI, Figure S2, M-
4 T). The elemental composition after chemical leaching determined by EDS was 62.9 ± 1.2 wt. %
5 Ir and 18.8 ± 8.0 wt. % Ni for NiIr-200-CL and 63.6 ± 16.6 wt. % Ir and 17.9 ± 9.0 wt. % Ni for
6 NiIr-300-CL. The weight percentages of Ir and Ni within NiIr-200-CL and NiIr-300-CL
7 determined from EDS analysis are in general agreement with data obtained by ICP. Analysis of
8 the solution used for the chemical leaching step determined that Ni and a small amount of Ir was
9 leached into the solution during the acid treatment. The acid treatment of NiIr-200 showed $58.4 \pm$
10 3.5 wt % of Ni and 1.7 ± 0.1 wt % Ir was leached into the solution, and acid treatment of NiIr-300
11 showed 62.9 ± 8.1 wt % Ni and 1.7 ± 0.1 wt % Ir was leached into the solution.
12
13
14
15
16
17
18
19
20
21
22
23

24 The ICP and EDS elemental analysis showed that Ni is present within the NiIr-200-CL and
25 NiIr-300-CL structures even after the chemical (acid) leaching step. While metallic Ir is
26 thermodynamically stable in acidic conditions,¹ metallic Ni is thermodynamically unstable in acid
27 as shown from Pourbaix diagrams.²⁶ Experiments of the stability of metallic Ni in acid have shown
28 that Ni dissolves into the electrolyte and forms passivating surface Ni oxides/hydroxides.²⁷⁻²⁸ The
29 very slow rate of NiO dissolution under acidic conditions (one monolayer per month at pH 1 and
30 60 °C) suggests that kinetics in addition to thermodynamics may affect the observed apparent
31 stability of NiO in acid.²⁶ In addition, the interaction of Ni with Ir may influence the stability of
32 metallic Ni in acid. The formation of Ir shells on IrNi solid solution alloy cores where the Ir layer
33 protects the non-noble Ni within the core was previously reported for core-shell nanoparticles.²⁹
34 A previous study reported residual Ni contents of 12 wt% Ni determined for mixed Ir-Ni oxide
35 where Ni was stabilized from dissolution in acidic electrolyte through interaction with Ir within
36 the oxide matrix.⁹
37
38
39
40
41
42
43
44
45
46
47
48
49
50
51
52
53
54
55
56
57
58
59
60

1
2
3 From ICP analysis, the NiIr-200-CL sample had a higher relative concentration of Ir, and
4 the NiIr-300-CL sample had a higher relative concentration of Ni. The differences in the Ni and
5 Ir compositions of NiIr-200-CL and NiIr-300-CL are attributed to differences in the structures of
6 the precursor materials before chemical leaching (NiIr-200 and NiIr-300) that influence the effect
7 of the chemical leaching treatment on the resulting structure. Although the NiIr-200 and NiIr-300
8 prior to chemical leaching showed similar relative percentages of Ir, Ni, and O within the structures
9 from EDS analysis (ESI, Figure S2,E-L), x-ray diffraction analysis and microscopy showed that a
10 NiO phase was present within NiIr-200, as discussed below. In contrast, NiIr-300 did not show the
11 presence of NiO. For the chemically leached samples, the higher amount of Ni within NiIr-300-
12 CL compared with NiIr-200-CL may be due to the higher temperature (300 °C) treatment resulting
13 in complete transformation of NiO that allows increased interaction of Ni with Ir which stabilizes
14 Ni from dissolution during the chemical leaching step. The comparison of the x-ray diffraction
15 (XRD) data of NiIr-200-CL and NiIr-300-CL also supports a higher degree of interaction of Ni
16 with Ir within the metallic phase of NiIr-300-CL, as discussed below.

17
18
19
20
21
22
23
24
25
26
27
28
29
30
31
32
33
34
35 **X-ray Diffraction Characterization.** The transformation of the materials upon the
36 synthesis steps was analyzed by XRD. The XRD patterns of NiO nanosheets, NiO:Ir, integrated
37 2D-NiIr structures treated at different temperatures (i.e. 200 and 300 °C), and the Ni-Ir structures
38 after chemical leaching, are shown in Figure 2. The black, blue, green and red lines at the bottom
39 represent the diffraction patterns of IrO₂, Ni, Ir and NiO standards respectively. The
40 crystallographic data is summarized in Table S1. Diffraction patterns were indexed to face-
41 centered cubic (FCC) phases. The XRD pattern for the NiO nanosheets shows reflections at 2θ
42 values of 36.82° and 42.98° corresponding to the (111) and (200) diffraction planes. The
43 deposition of iridium onto the NiO nanosheets (i.e. NiO:Ir) did not show any observable changes
44
45
46
47
48
49
50
51
52
53
54
55
56
57
58
59
60

in the XRD pattern, which is consistent with no significant morphology changes in the NiO nanosheets from the SEM images (Figure 1C). Although the EDS mapping of NiO:Ir clearly showed the presence of Ir (ESI, Figure S2B), no diffraction peaks associated with iridium or iridium oxide phases were observed within the XRD pattern, which suggests the presence of an atomically distributed Ir or small Ir clusters rather than a highly ordered Ir phase. Our previous investigation of Pt deposited on Ni(OH)₂ nanosheets using a similar approach showed the presence of some atomically distributed Pt in addition to Pt nanoparticles.¹⁹

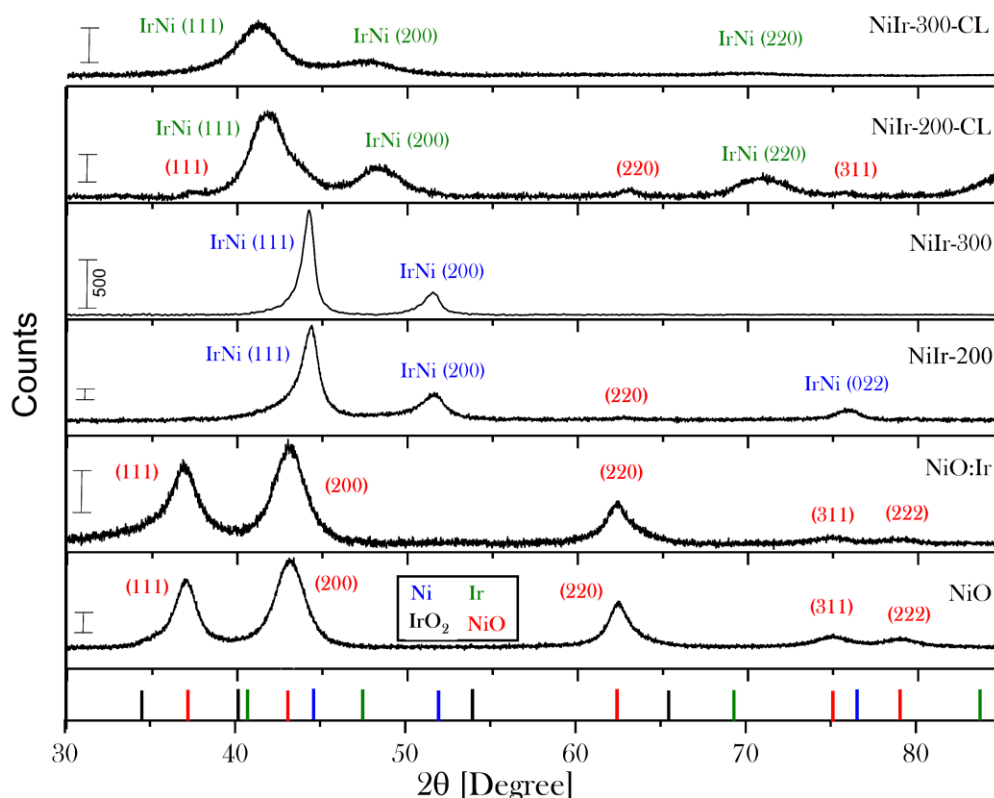


Figure 2. X-ray diffraction patterns (XRD) of precursor materials (NiO nanosheets and NiO:Ir) and Ni-Ir materials after different thermal and chemical treatments (NiIr-200, NiIr-300, NiIr-200-CL, and NiIr-300-CL). Vertical lines denote reference patterns of nickel (blue), nickel oxide (red), iridium (green) and iridium oxide (black).

1
2
3 After thermal treatment under a H₂/Ar atmosphere, significant structural modifications
4 were observed in the XRD patterns. The thermally treated samples showed two main XRD peaks
5
6 at 2θ values of 43.98° and 51.09° for NiIr-200 and peaks at 44.09° and 51.33° for NiIr-300
7
8 corresponding to the (111) and (200) planes of metallic Ni. The 2θ values were slightly lowered
9
10 compared with the values for a pure metallic Ni phase (2θ values of 44.34° and 51.67°) which is
11
12 consistent with a cell volume expansion due to the incorporation of Ir within the structure and the
13
14 formation of a Ni-rich Ni-Ir solid solution. In addition, NiIr-200 shows the presence of NiO (111)
15
16 and (220) peaks at small relative intensities indicating the presence of a segregated NiO phase as
17
18 a result of an incomplete transformation NiO to metallic Ni within the NiIr-200 material. In
19
20 contrast, no reflections due to NiO were observed for the sample heated to 300 °C, NiIr-300.
21
22
23
24
25

26
27 The XRD peaks of NiIr-300 were shifted toward higher 2θ values and were narrower
28
29 compared with NiIr-200 which suggests a relatively higher degree of Ir incorporated within the Ni
30
31 structure, as well as an increase of the crystallite size and/or diminishing of local lattice strain
32
33 (microstrain) due to thermally induced relaxation.³⁰ The structural differences between NiIr-200
34
35 and NiIr-300 are important because they influence the changes during the subsequent Ni leaching
36
37 process and resulting structural surface reconstruction and pore formation that occur during the
38
39 chemical leaching step.
40
41
42

43 After the chemical leaching step, the partial leaching of Ni results in bulk and surface
44
45 atomic reconfiguration, which significantly changed the XRD patterns of NiIr-200-CL and NiIr-
46
47 300-CL compared with their precursor materials, NiIr-200 and NiIr-300, respectively. In general,
48
49 the dissolution of the non-noble metal (i.e. Ni) resulted in a significant cell volume expansion, as
50
51 demonstrated by shifting of peaks within NiIr-200-CL and NiIr-300-CL to lower 2θ° values with
52
53 respect to the samples before acid leaching (i.e. NiIr-200 and NiIr-300). The chemical leaching
54
55
56
57
58
59
60

1
2
3 step resulted in peaks with $2\theta^\circ$ values in the range of metallic Ir, however the $2\theta^\circ$ values remained
4
5 at higher angles compared with pure metallic Ir which is consistent with a compressed cell volume
6
7 due to the presence of residual Ni and suggests the formation of an Ir-rich Ir-Ni solid solution.
8
9 Even after the chemical leaching step, the presence of remaining Ni within the NiIr-200-CL and
10
11 NiIr-300-CL structures is supported by XRD data, EDS analysis (Figure S2,M-T) and ICP data.
12
13 The presence of Ni within NiIr-200-CL and NiIr-300-CL (after chemical leaching) may be due to
14
15 the interaction with Ir, as supported by prior work^{9,29} as discussed above.
16
17
18

19 The comparison of the XRD patterns of NiIr-200-CL and NiIr-300-CL reveals appreciable
20
21 differences between the samples. Within NiIr-200-CL, NiO peaks were still observed suggesting
22
23 a relative stability of some NiO, as described above, using the conditions utilized for the acid
24
25 leaching step. In addition, the lower $2\theta^\circ$ values of the (111) peak of NiIr-300-CL (41.21°)
26
27 compared with NiIr-200-CL (41.73°) is consistent with different local Ni-Ir crystal composition
28
29 within the samples and suggests a higher relative Ni content within NiIr-300-CL. The broader
30
31 width of the (111) peak within NiIr-300-CL compared with NiIr-200-CL also indicates differences
32
33 in the particle size and/or microstrain between the samples.³⁰ A previous study reported the
34
35 formation of atomic vacancies in the top most and near-surface layers caused by Ni leaching as
36
37 well as higher amounts of residual Ni within acid leached (dealloyed) NiPt alloys resulted in higher
38
39 degrees of microstrain.³¹ For NiIr-200-CL and NiIr-300-CL, the acid leaching step also causes
40
41 significant increases in surface area (ESI, Table S2) which may contribute to microstrain within
42
43 the near surface layers.
44
45
46
47
48

49 **Scanning Transmission Electron Microscopy Characterization of Thermally-treated**
50
51 **and Chemically Leached Samples.** A detailed characterization of the morphology and atomic
52
53 surface reconstruction caused by hydrogen treatment and acid leaching was carried out by a
54
55
56
57

1
2
3 combined analysis of high angle annular dark-field scanning transmission electron microscopy
4 (HAADF-STEM), energy-dispersive x-ray spectroscopy (EDX), and tomography STEM. The
5
6 (HAADF-STEM), energy-dispersive x-ray spectroscopy (EDX), and tomography STEM. The
7
8 microscopy analysis focused on the sample heated to 200 °C (NiIr-200) and after chemical leaching
9
10 (NiIr-200-CL) since this sample showed the highest OER activity.
11

12 Shown in Figure 3A-F are HAADF-STEM images, elemental mapping, and line scans of
13
14 the NiIr-200 sample after thermal treatment under H₂/Ar at 200° C. The HAADF-STEM image
15
16 (Figure 3A) shows an interconnected matrix, and elemental mapping (Figure 3B-D) displays a
17
18 uniform distribution of Ir, Ni, and O within the sample. The HAADF-STEM image (Figure 3E)
19
20 shows the interconnected network is composed of Ir-Ni alloy nanoparticles segregated within a
21
22 highly porous Ni/NiO nanoarchitecture, as supported by the contrast and lattice spacing (ESI,
23
24 Figure S4A). The linear profile (Figure 3F) shows a brighter region with a lattice distance around
25
26 0.218 nm, corresponding to the (111) lattice planes of a NiIr-rich solid solution, and this distance
27
28 increases to 0.240 nm towards the surface, which can be interpreted as formation of a NiO layer
29
30 covering the surface. Similar features were observed on our previous Ni-Pt catalysts heated under
31
32 hydrogen atmospheres.¹⁹ The HAADF-STEM images and analysis of the lattice distances indicate
33
34 the sample is heterogeneous and includes the presence of domains with different surface
35
36 compositions: domains of Ir-rich Ni-Ir solid solution (~0.218 nm), domains of a Ni-rich Ni-Ir solid
37
38 solution (~0.205 nm), and domains of NiO (~0.238 nm) (ESI, Figure S4A). The presence of NiO
39
40 domains is consistent with XRD data (Figure 2).
41
42
43
44
45
46
47
48
49
50
51
52
53
54
55
56
57
58
59
60

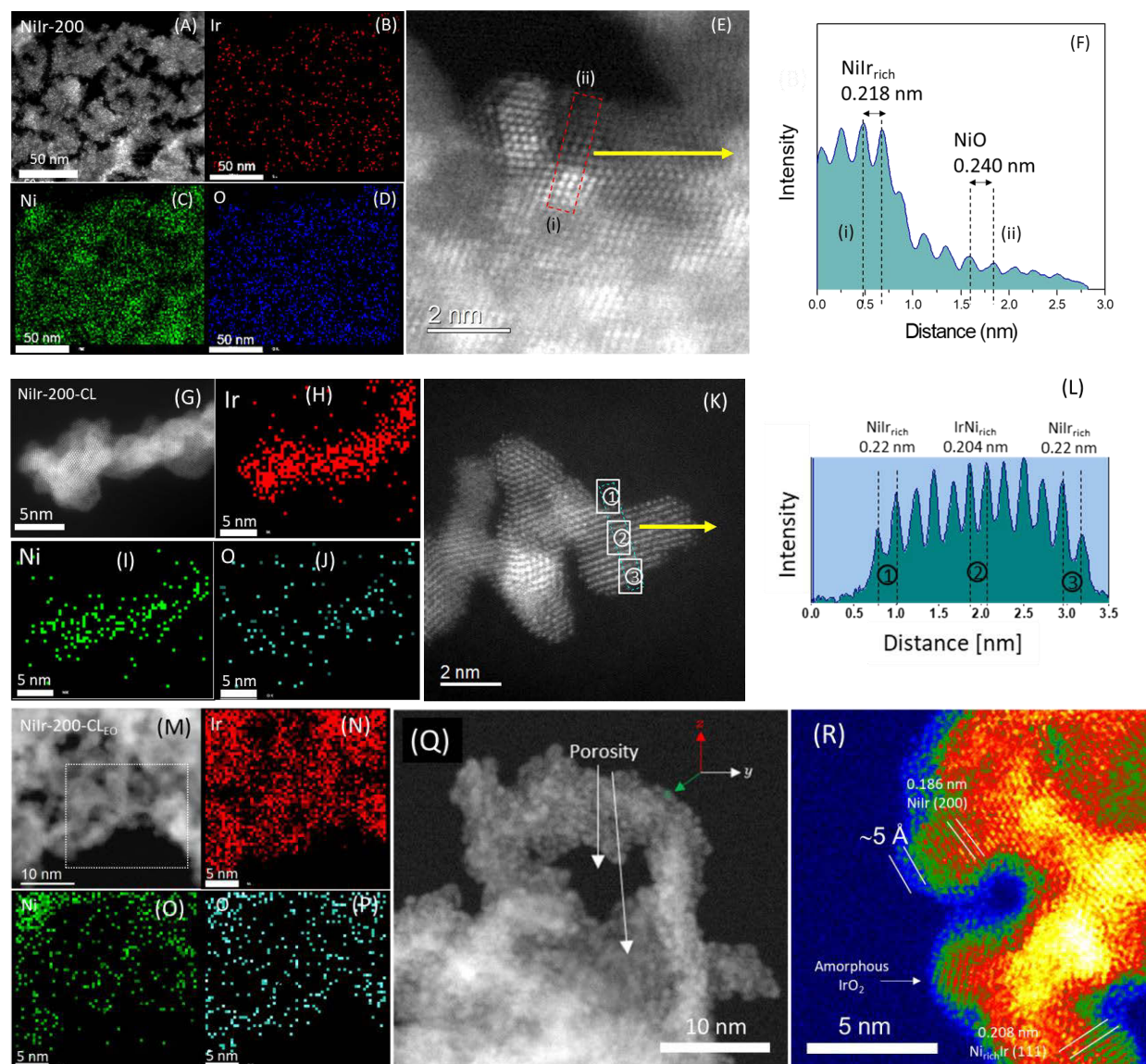


Figure 3. High angle annular dark-field scanning transmission electron microscopy (HAADF-STEM), energy-dispersive x-ray spectroscopy (EDS), line scans, and tomography STEM of (A-F) NiIr-200 (after thermal treatment at 200 °C in H₂/Ar); (G-L) NiIr-200-CL (after chemical leaching), and (M-R) NiIr-200-CL_{EO} (after electrochemical oxidation).

The chemical leaching step resulted in a surface and bulk reorganization of the material. The acid treatment promoted almost entirely the removal of Ni/NiO leaving an enriched-Ir surface; however, a thorough analysis of the structure still revealed the presence of NiO over a very small fraction of the material (ESI, Figure S4C), in line with the evidence obtained from XRD and XPS

1
2
3 as discussed below. The HAADF-STEM images, elemental mapping, and line scans for NiIr-200-
4
5 CL (after the chemical leaching step in 0.05 M HNO₃) are shown in Figure 3G-L. After the
6
7 chemical leaching, the presence of Ni distributed within the structure is supported by EDS mapping
8
9 (Figure 3I) and line scans (ESI, Figure S4D-E). The presence of a metallic Ir-Ni solid solution
10
11 after chemical leaching is consistent with the XRD data (Figure 2) that shows XRD peaks at higher
12
13 2θ° values relative to metallic Ir due to the interaction of Ni within the structure. The HAADF-
14
15 STEM image and analysis of lattice plane distances from the line scan of NiIr-200-CL (Figure 3K-
16
17 L) show a heterogenous structure that consists of NiIr_{rich} phase at the surface (0.22 nm distance)
18
19 and a Ni_{rich}Ir phase (0.204 nm distance) within the core, supporting the presence of a Ni depleted
20
21 surface region and higher amounts of Ni within the core. The presence of different surface and
22
23 core structures within NiIr-200-CL indicates a surface segregation process occurs. Surface
24
25 segregation has been previously observed for nickel-based bimetallic alloy nanoparticles and has
26
27 been shown to depend on surface energy and be influenced by temperature, chemical composition,
28
29 miscibility, particle shape and size, and chemical environment.³²⁻³⁴ The surface segregation of Ir
30
31 within IrNi core-shell nanoparticles supported on carbon was previously reported.²⁹
32
33
34
35
36
37

38 After the chemical leaching step, the porous nanoarchitecture was maintained (ESI, Figure
39
40 S4B). The removal of Ni from the structure due to chemical leaching also resulted in increasing
41
42 the porosity of the material from analysis of the Brunauer–Emmett–Teller (BET) surface area that
43
44 showed the surface area increased from 52 ± 3 m² g⁻¹ for NiIr-200 to 72 ± 3 m² g⁻¹ for NiIr-200-
45
46 CL (ESI, Figure S5 and Table S2). The chemically leached sample, NiIr-200-CL, also showed a
47
48 higher mean pore diameter of 22 ± 2 nm and cumulative pore volume of 0.39 ± 0.18 cm³ g⁻¹
49
50 compared with the as-prepared NiIr-200 (mean pore diameter of 16 ± 1 nm and cumulative pore
51
52 volume of 0.21 ± 0.01 cm³ g⁻¹).
53
54
55
56
57
58
59
60

X-ray photoelectron spectroscopy. X-ray photoelectron spectroscopy (XPS) was used to characterize the surface structure of the chemically leached catalysts and evaluate the effects of temperature on the surface structure. Based on the inelastic mean free path of the O *1s* and Ni *2p* photoelectrons, a significant proportion of the XPS signal intensity arises from the top few nanometers of the surface.³⁵ The analysis of atomic percentages of Ir, Ni, and O within the surface region obtained from XPS are shown in Table 1. The XPS data supports that NiIr-200-CL contains a higher relative atomic percent of Ir within the surface region, and NiIr-300-CL contains a higher relative atomic percent of Ni within the surface region; however the values are within the range of experimental error. The atomic percentages of Ir, Ni and O within the surface region as determined by XPS are within experimental error of the atomic percentages determined from EDS analysis (ESI, Table S3). The higher relative atomic percent of Ni within the surface region of NiIr-300-CL compared with NiIr-200-CL is consistent with the higher weight percent of bulk Ni within NiIr-300-CL determined from ICP analysis. As discussed above, the higher amount of Ni within NiIr-300-CL compared with NiIr-200-CL may result from the higher temperature (300 °C) treatment resulting in complete transformation of NiO that allows increased interaction of Ni with Ir that stabilizes Ni from dissolution during the chemical leaching step.

Table 1. Relative atomic percentages of iridium, nickel and oxygen within the surface region from analysis of x-ray photoelectron spectra.

Sample	Element	Atomic % determined from XPS
NiIr-200-CL	Iridium	25 ± 15
	Nickel	14 ± 11
	Oxygen	61 ± 4
NiIr-300-CL	Iridium	13 ± 3
	Nickel	26 ± 3
	Oxygen	60 ± 1

1
2
3 Peak fitting was performed to determine the presence and relative atomic percentages of
4 metallic, oxide, and hydroxide surface species within the NiIr-200-CL and NiIr-300-CL samples.
5
6
7 Peak fitting of the Ir $4f$ / Ni $3p$, Ni $2p_{3/2}$ and O $1s$ regions was performed by including peaks with
8
9 binding energies reported for metallic Ir, IrO₂, and NiO based on prior studies.³⁵⁻³⁸ Shown in Figure
10
11 4 are the x-ray photoelectron spectra of NiIr-200-CL and NiIr-300-CL in the Ir $4f$ / Ni $3p$, Ni $2p_{3/2}$
12
13 and O $1s$ spectral regions. Details of the peak binding energies, relative peak areas, and
14
15 assignments are provided in Table 2. Peaks in the Ir $4f$ region show characteristic doublets of $4f_{7/2}$
16
17 and $4f_{5/2}$ peaks due to spin-orbit splitting, and peaks arising from metallic Ir, anhydrous IrO₂,
18
19 hydrous IrO₂ have been previously shown to occur at different binding energies.³⁶ In addition, the
20
21 binding energies of Ni $3p$ peaks are within the Ir $4f$ spectral window.³⁷ The XPS spectra of NiIr-
22
23 200-CL and NiIr-300-CL in the Ir $4f$ / Ni $3p$ region (Figure 4A) show the presence of peaks with
24
25 binding energies that are consistent with metallic Ir (labelled Ir-1 and Ir-2), anhydrous IrO₂
26
27 (labelled IrO₂-A1 and IrO₂-A2), and hydrous IrO₂ (IrO₂-H1 and IrO₂-H2).³⁶ The comparison of
28
29 fitted peaks of the sample heated to 200 °C (NiIr-200-CL) and 300 °C (NiIr-300-CL) shows that
30
31 the sample heated to 200 °C has a higher relative concentration (~2 times higher peak area) of
32
33 hydrous IrO₂ (peaks at 62.5 and 65.5 eV) within the surface region (Table 2). Hydrous IrO₂ has
34
35 surface hydroxides present,³⁶ and iridium hydroxo (Ir-OH) surface species have been reported to
36
37 be strongly linked to OER activity based on a prior study.³⁹
38
39
40
41
42
43
44
45
46
47
48
49
50
51
52
53
54
55
56
57
58
59
60

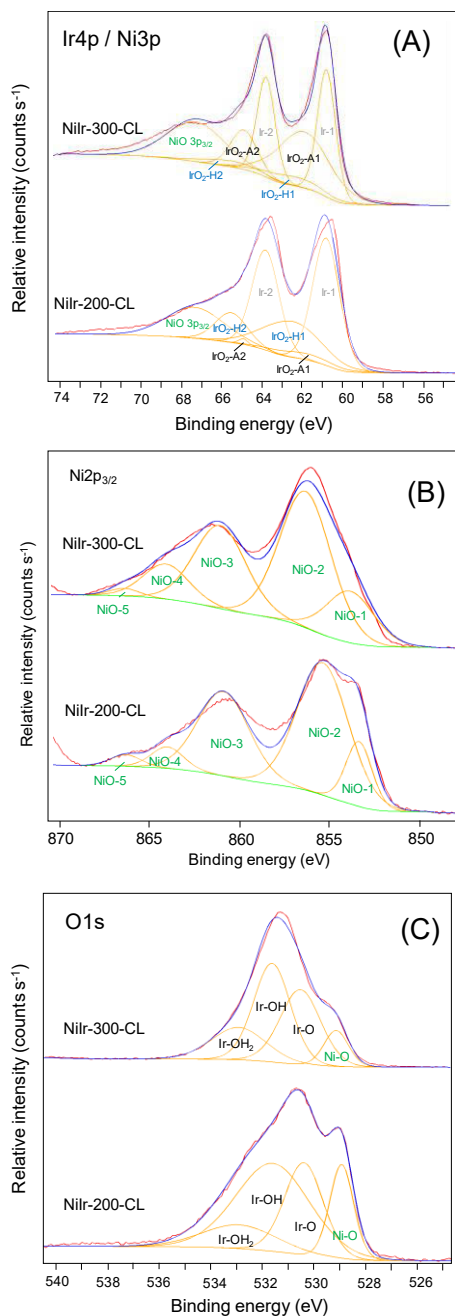


Figure 4. X-ray photoelectron spectra of NiIr-200-CL and NiIr-300-CL in the Ir 4f / Ni 3p (A), Ni 2p_{3/2} (B), and O 1s (C) regions; peaks obtained from fitting analysis are included and details are provided in the text.

The XPS spectra of NiIr-200-CL and NiIr-300-CL within the Ni 2p_{3/2} region (Figure 4B) shows the presence of a set of peaks due to multiplet splitting with five peaks previously reported for NiO in the Ni 2p_{3/2} region.³⁵ The observed binding energies within both NiIr-200-CL and NiIr-

1
2
3 300-CL are consistent with the binding energies of NiO³⁵ which supports that nickel oxide is
4 present within the surface region of both samples. The presence of NiO is further supported by the
5
6 observed binding energy of Ni $3p_{3/2}$ peaks within NiIr-200-CL and NiIr-300-CL (Figure 4A) which
7
8 are consistent with the binding energy of the Ni $3p_{3/2}$ peak of NiO.³⁷ The effects of including
9
10 additional peak at 852.6 eV corresponding to metallic Ni³⁵ was also evaluated since STEM
11
12 measurements (Figure 3K-L) supported the presence of a Ir-rich IrNi alloy. The addition of the
13
14 852.6 eV peak within the peak fitting analysis resulted in a relative peak area of less than 2 % for
15
16 this peak, and therefore the 852.6 eV peak was not included in the fitting analysis of the Ni $2p_{3/2}$
17
18 region, described above. The likelihood of binding energy shifts of metallic Ni within the Ni-Ir
19
20 alloy phase, the multiplet splitting of Ni $2p_{3/2}$ peaks, and the similar range of binding energies for
21
22 metallic Ni (852.6 eV, 856.3 eV, 858.7 eV)³⁵ and NiO (Table 2) complicate the peak fitting
23
24 analysis of the Ni $2p_{3/2}$ region. The presence of NiO within the surface region of NiIr-200-CL and
25
26 NiIr-300-CL is clearly supported by the presence of the higher 864.0 and 866.3 eV peaks which
27
28 are not present for metallic Ni.^{35,38}
29
30
31
32
33
34

35 The O $1s$ region (Figure 4C) shows the presence of peaks with binding energies that are
36
37 consistent with hydrated iridium oxide, with peaks attributed to iridium oxide (labelled Ir-O),
38
39 iridium hydroxide (labelled Ir-OH), and water (labelled Ir-OH₂).³⁶ In addition, the peak observed
40
41 at a lower binding energy of 529.2 eV (labeled Ni-O) is in the range of the reported O $1s$ binding
42
43 energy of NiO (529.6 eV).³⁷ The O $1s$ regions of NiIr-200-CL and NiIr-300-CL show differences
44
45 in the relative peak areas of the Ir-O, Ir-OH, Ir-OH₂, and NiO peaks (Figure 4C and Table 2).
46
47
48

49 Overall, the XPS data supports that the surface region of NiIr-200-CL and NiIr-300-CL
50
51 contains metallic Ir, anhydrous IrO₂, hydrous IrO₂, and NiO in the surface region. From analysis
52
53 of the Ir $4f$ / Ni $3p$, Ni $2p_{3/2}$ and O $1s$ regions, the temperature used for thermal reduction under
54
55
56
57

hydrogen (either 200 °C or 300 °C) resulted in changes to the surface structure. Comparing the XPS spectra of NiIr-200-CL and NiIr-300-CL, two noticeable trends are observed: the NiIr-200-CL sample has a higher relative concentration of hydroxides and NiO in the surface region compared with NiIr-300-CL. The effect of temperature was previously reported as a factor that affected surface segregation of nickel-based bimetallic alloy nanoparticles.^{32,34} The different surface structures of NiIr-200-CL and NiIr-300-CL influence their OER activities and stabilities, as discussed below.

Table 2. Peaks, binding energies and relative areas from fitting analysis of x-ray photoelectron spectra and assignment of surface species. The relative error in binding energies is estimated as ± 0.1 eV.

Region	Peak Label	NiIr-200-CL		NiIr-300-CL		Assignment ³⁵⁻³⁸
		Binding energy (eV)	Relative area (%)	Binding energy (eV)	Relative area (%)	
Ir 4f/ Ni 3p	Ir-1	60.8	15.9	60.8	17.8	Ir 4f _{7/2} , Ir metal
	Ir-2	63.8	12.3	63.8	14.9	Ir 4f _{5/2} , Ir metal
	IrO ₂ -A1	61.9	22.8	61.9	23.0	Ir 4f _{7/2} , IrO ₂ (anhydrous)
	IrO ₂ -A2	64.9	19.2	64.9	14.0	Ir 4f _{5/2} , IrO ₂ (anhydrous)
	IrO ₂ -H1	62.5	13.3	62.5	7.8	Ir 4f _{7/2} , IrO ₂ (hydrous)
	IrO ₂ -H2	65.5	4.2	65.5	2.2	Ir 4f _{5/2} , IrO ₂ (hydrous)
	NiO	67.3	12.1	67.3	20.8	Ni 3p _{3/2} , NiO
Ni 2p _{3/2}	NiO-1	853.6	12.3	853.7	13.0	Ni 2p _{3/2} , NiO
	NiO-2	855.4	49.0	855.4	43.8	Ni 2p _{3/2} , NiO
	NiO-3	860.9	31.3	860.9	30.1	Ni 2p _{3/2} , NiO
	NiO-4	864.0	4.9	864.0	10.7	Ni 2p _{3/2} , NiO
	NiO-5	866.3	2.5	866.3	2.4	Ni 2p _{3/2} , NiO
O 1s	Ni-O	529.6	16.5	529.5	7.3	O1s, Ni-O
	Ir-O	530.5	24.5	530.5	44.8	O1s, Ir-O
	Ir-OH	531.6	33.1	531.6	31.2	O1s, Ir-OH
	Ir-OH ₂	532.9	25.9	532.9	16.8	O1s, Ir-OH ₂

Cyclic Voltammetric Analysis. Cyclic voltammetry (CV) was used to characterize the surface of the electrocatalyst materials after chemical leaching. Shown in Figure 5A are the CVs obtained for NiIr-200-CL and NiIr-300-CL after electrochemical conditioning at a low potential

1
2
3 range (i.e. $E \leq 1.0 V_{RHE}$) in O_2 -free 0.1 M $HClO_4$. The materials exhibit metallic features within
4
5 the CVs with distinct H-adsorption and H-desorption features observed at low potentials ($E \leq 0.3$
6
7 V_{RHE}) characteristic of hydrogen underpotential deposition (H_{upd}) on metallic Ir.^{25,40} The presence
8
9 of metallic Ir at the surface is supported by the presence of H-adsorption and H-desorption features
10
11 and also further supported by XPS measurements that show metallic Ir at the surface region (Figure
12
13 4) and STEM images that show lattice spacings that are consistent with a metallic phase (Figure
14
15 3K-L). Although the integrated charge within the H_{upd} region has been used to determine the ECSA
16
17 of metallic Ir,²⁵ this analysis was not used in this case since the anodic scan showed a cathodic
18
19 (negative) current around $0.3 V_{RHE}$ (Figure 5A). Similar features within the H_{upd} and
20
21 electrochemical double layer voltage regions were previously observed and attributed to the
22
23 reduction of perchlorate on metallic Ir⁴¹⁻⁴² which complicates the determination of the
24
25 electrochemical surface area (ECSA) from the integrated charge within the H_{upd} region for metallic
26
27 Ir using electrolytes containing perchlorate anions.
28
29
30
31
32
33
34
35
36
37
38
39
40
41
42
43
44
45
46
47
48
49
50
51
52
53
54
55
56
57
58
59
60

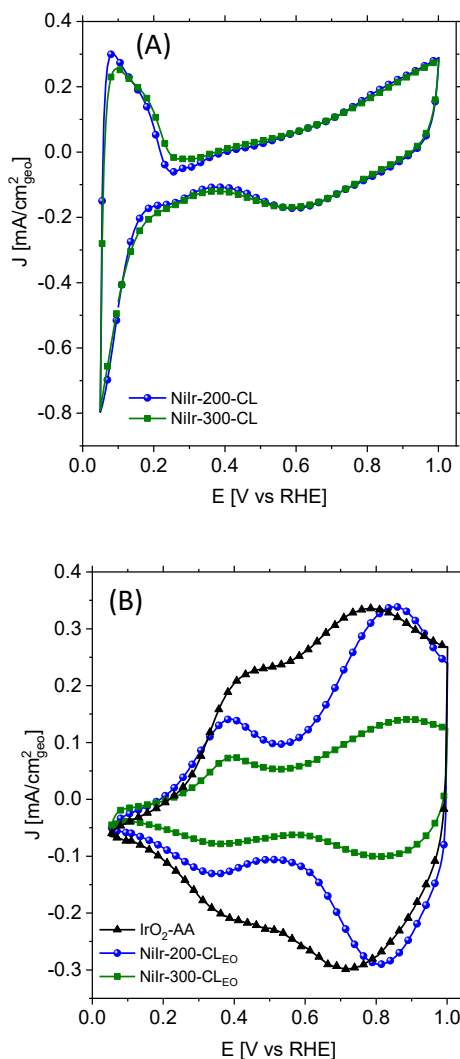


Figure 5. (A) Initial cyclic voltammograms (CVs) of NiIr-200-CL and NiIr-300-CL; (B) Representative CVs of NiIr-200-CL_{EO} and NiIr-300-CL_{EO} after electrochemical conditioning and OER activity evaluation carried out before stability test; CV of IrO₂-AA (Alfa Aesar) included for reference; CVs obtained in Ar-saturated 0.1 M HClO₄ using a scan rate of 100 mV s⁻¹ obtained with electrode loadings of L_{Ir}=11.7 μg_{Ir} cm⁻²_{geo} (NiIr-200-CL), 9.1 μg_{Ir} cm⁻²_{geo} (NiIr-300-CL) and 11.6 μg_{Ir} cm⁻²_{geo} (IrO₂-AA).

In addition to H-adsorption and H-desorption features within the CV, oxidation/reduction peaks due to reversible IrO_x formation/reduction at $E \geq 0.5 V_{RHE}$ ⁴⁰ were observed. We consider that the observed IrO_x redox peaks primarily result from the transformation of metallic Ir to IrO_x, as previously observed within a prior CVs of thin film metallic Ir.⁴⁰ Analysis of the XPS data

1
2
3 supports that in addition to metallic Ir, there are some Ir oxide/hydroxide species in the surface
4 region (Figure 4) which may also contribute to some of the observed surface oxide current. Within
5 the CVs of NiIr-200-CL and NiIr-300-CL (Figure 5A), the relative peak areas of the surface oxide
6 features and H-desorption features are similar. A prior study of CVs of thin film metallic Ir showed
7 a lower relative peak area of surface oxide features compared with H-desorption features⁴⁰ which
8 may indicate that in addition to surface oxides formed from metallic Ir some existing surface
9 oxide/hydroxide species may contribute to the current response within the CVs of NiIr-200-CL
10 and NiIr-300-CL. The presence of metallic Ni at the topmost surface of the catalyst was not
11 considered since metallic Ni is thermodynamically unstable under anodic potentials in acidic
12 conditions as shown from Pourbaix diagrams²⁶ and prior experiments.²⁷⁻²⁸ In addition, no
13 discernable peaks commonly associated to the electrooxidation of unstable Ni atoms at the
14 surface⁴³ were observed, which supports that a stable Ir-rich surface is formed after the chemical
15 leaching step, which is consistent with information obtained from other experimental
16 measurements (i.e. XRD, XPS and STEM) as discussed above.

17
18
19 We further characterized the surface structure by performing electrochemical carbon
20 monoxide (CO) oxidation (CO stripping). CO oxidation has been established as a surface sensitive
21 reaction, and changes in morphology and/or surface species can influence the oxidation behavior.⁴⁴
22 The surface adsorption and subsequent oxidation of CO has been observed on a number of metals
23 including Pt and Ir.^{25,44} Since the surface of the NiIr-200-CL and NiIr-300-CL was predominately
24 metallic as evidenced by the significant H_{upd} features, we utilized CO oxidation to evaluate the
25 ECSA of metallic Ir (ECSA_{Ir}) for the catalysts.²⁵ For the NiIr 2D nanoframes, the average CO
26 oxidation potential on NiIr-200-CL was lower than that of NiIr-300-CL (ESI, Figure S6), which
27 is attributed to differences in the surface structure as supported by XPS measurements (Figure 4).

1
2
3 The integrated area of the CO oxidation peak (ESI, Figure S6) was used to determine the
4 electrochemical surface area of metallic Ir (ECSA_{Ir}) using a coulombic charge of 358 $\mu\text{C cm}_{\text{Ir}}^{-2}$.²⁵
5
6 For NiIr-200-CL, the ECSA_{Ir} values determined from CO oxidation ($49.1 \pm 9.5 \text{ m}^2 \text{ g}^{-1}$) was slightly
7
8 lower than the BET surface area ($71.5 \pm 3 \text{ m}^2 \text{ g}^{-1}$); however for NiIr-200-CL, the ECSA_{Ir} ($65.5 \pm$
9
10 $11.3 \text{ m}^2 \text{ g}^{-1}$) was comparable to the BET surface area ($69.5 \pm 3.8 \text{ m}^2 \text{ g}^{-1}$) (ESI, Table S2). For NiIr-
11
12 300-CL, the similar BET surface area compared with ECSA_{Ir} suggests that the surface is
13
14 predominantly metallic Ir. The slightly lower ECSA_{Ir} for NiIr-200-CL may be related to (i) the
15
16 presence of a segregated NiO phase (Figure 2) which contributes to the BET surface area but not
17
18 to the ECSA and/or (ii) the higher relative concentration of surface oxide/hydroxide species as
19
20 determined from XPS analysis as described above. While CO oxidation is effective at probing
21
22 metallic Ir at the surface, surface oxide/hydroxides would not be probed by CO oxidation since a
23
24 prior study showed that CO was not adsorbed on Ir oxide nanoparticles and CO oxidation was
25
26 ineffective on oxides.²⁵
27
28
29
30
31
32

33 From our initial OER testing, we determined that the surface of the electrocatalyst was
34 altered after cycling to the high potentials required for the oxygen evolution reaction. Therefore,
35 an electrochemical oxidation step (sixty CV scans between 0.05-1.5 V_{RHE}) was utilized to allow
36 electrochemical surface oxidation prior to OER evaluation, since this surface most closely
37 represents the catalyst under OER potentials. For clarity, catalysts are labeled with the suffix “EO”
38 (i.e. NiIr-200-CL_{EO} and NiIr-300-CL_{EO}) to designate catalysts treated with the electrochemical
39 oxidation protocol. As shown in Figure 5B, following successive CV scans from 0.05 to 1.5 V_{RHE}
40 and OER evaluation, the features observed within the cyclic voltammograms of NiIr-200-CL_{EO}
41 and NiIr-300-CL_{EO} are consistent with a hydroxide/oxide surface. After the electrochemical
42 oxidation step, peaks due to H_{upd} features were not clearly evident for both the NiIr-200-CL_{EO} and
43
44
45
46
47
48
49
50
51
52
53
54
55
56
57
58
59
60

1
2
3 Ni-Ir-300-CL_{EO} samples. The comparison of the initial CV (Figure 5A) that shows features that
4 indicate a metallic surface with the CV after electrochemical oxidation (Figure 5B) supports that
5 the initial metallic surface was predominantly transformed to a hydroxide/oxide surface, which is
6 similar to the findings of reports of planar metallic Ir surfaces.⁴⁰ The anodic peaks centered ~0.37-
7 0.42 V_{RHE} within the CVs (Figure 5B) are attributed to the formation of hydrated Ir³⁺-OH species
8 based on prior work,³⁹ while the peak at ~0.8 V_{RHE}, is attributed to the transition from Ir³⁺ to Ir⁴⁺
9 species.⁴⁵⁻⁴⁷ Peaks at similar potentials have been observed on iridium disk electrodes that were
10 electrochemically oxidized.⁴⁰ We note that the presence and nature of hydroxide surface species
11 may be particularly important since reported OER mechanisms involves hydroxides,³ as discussed
12 further below. We also note that after the electrochemical oxidation step, the CVs of the samples
13 heated to 200 °C and 300 °C showed the presence of oxide and hydroxides peaks with different
14 relative peak areas depending on the treatment temperature and with different relative peak
15 positions compared with IrO₂ which supports different surface structures within the catalysts. To
16 further analyze the CV features, peak deconvolution of the anodic peaks of the CV of the
17 electrochemical oxidation step for NiIr-200-CL_{EO} and NiIr-300-CL_{EO} was performed to identify
18 the number of peaks, peak potentials, and relative peak areas (ESI, Figure S7 and supporting text).
19 The peak deconvolution supported the presence of an additional feature at 0.47-0.56 V_{RHE} (peak
20 “A₂”) within the NiIr-200-CL_{EO} and Ni-Ir-300-CL_{EO} materials which was not present in the IrO₂-
21 AA sample that may be due to a different surface structure present within the materials.⁴⁸

22
23
24
25
26
27
28
29
30
31
32
33
34
35
36
37
38
39
40
41
42
43
44
45
46
47
48
49
50
51
52
53
54
55
56
57
58
59
60

Based on the changes in the surface after the electrochemical oxidation step observed by CV that showed that the initially predominately metallic surface was changed to an oxide/hydroxide surface (Figure 5), we further evaluated the ECSA of the catalysts after the electrochemical oxidation step. As discussed above, although CO oxidation provides reasonable

1
2
3 ECSAs for metallic Ir, CO oxidation was ineffective on oxide surfaces.²⁵ Pseudocapacitance
4
5 measurements have been previously utilized to determine the electrochemical surface area of
6
7 iridium oxides.^{24,49-50} We measured the pseudocapacitive charge from 0.3 to 1.25 V_{RHE} at a scan
8
9 rate of 50 mV s⁻¹ and utilized the previously determined coulombic conversion factor of
10
11 596 μC cm_{IrO₂}⁻² obtained under similar experimental conditions²⁴ to calculate the IrO₂
12
13 electrochemical surface area (ECSA_{IrO₂}) of IrO₂-AA_{EO}, NiIr-200-CL_{EO} and Ni-Ir-300-CL_{EO} (ESI,
14
15 Figure S8). Our analysis also included subtraction of the current contribution from the Au current
16
17 collector. Using this approach, we determined an ECSA_{IrO₂} of 25.3 ± 1.5 m² g⁻¹ for IrO₂-AA_{EO}
18
19 which is similar to the previously reported ECSA of 28.7 m² g⁻¹ determined using Hg_{upd} and also
20
21 similar to the reported BET surface area of 35 m² g⁻¹ for this material.²⁵ The calculated ECSA_{IrO₂}
22
23 values for NiIr-200-CL_{EO} and Ni-Ir-300-CL_{EO} were 11.5 ± 4.5 and 12.4 ± 2.3 m² g⁻¹ respectively.
24
25 These ECSA_{IrO₂} values are similar to ECSA values obtained for NiIr and CoIr nanowires with high
26
27 relative Ir concentrations (~15 m² g⁻¹).⁵
28
29
30
31
32
33

34 The calculated ECSA_{IrO₂} (after electrochemical oxidation) is considerably lower than the
35
36 calculated ECSA_{Ir} (before electrochemical oxidation). It is possible that partial agglomeration of
37
38 particles within 3D structure and/or growth of the oxide/hydroxide film, as described below, may
39
40 hinder electrolyte access to smaller pores within the 3D structure.²²⁻²³ In addition, a number of
41
42 factors may influence the determined values for ECSA_{Ir} and ECSA_{IrO₂}. Different coulombic charge
43
44 conversion factors have been reported for carbon monoxide oxidation on Ir²⁵ which would alter
45
46 the calculated ECSA_{Ir}. In addition, prior studies reported that scan rate and film thickness were
47
48 found to influence charge storage in iridium oxides^{49,51} which may affect the determined value for
49
50 ECSA_{IrO₂}. Further analysis is needed to determine how these factors may affect the ESCA of Ir
51
52 oxide-based 3D structures.
53
54
55
56
57
58
59
60

1
2
3 **Scanning Transmission Electron Microscopy Characterization on NiIr-200CL_{EO}**
4 **after Electrochemical Oxidation.** Based on the CV analysis that showed changes after
5 electrochemical oxidation, we analyzed the NiIr-200CL_{EO} sample (i.e. NiIr-200-CL after the
6 electrochemical oxidation procedure) using ex-situ high resolution STEM tomography and
7 electron energy loss spectroscopy (EELS) measurements to probe changes in the structure after
8 electrochemical oxidation. The measurements after treatment at high potentials (1.5 V_{RHE}) are
9 particularly useful to characterize the actual catalyst structure that is present during the oxygen
10 evolution reaction.
11
12
13
14
15
16
17
18
19
20

21 A slice of a three-dimensional (3D) STEM tomography of NiIr-200-CL_{EO} is shown in
22 Figure 3Q and indicates the 3D network consisting of interconnected Ir-Ni domains and a pore
23 structure containing mesopores (2-50 nm) and micropores (<2 nm) was maintained after cycling
24 at high potentials (1.5 V_{RHE}). The catalyst nanoarchitecture can maximize the availability of highly
25 catalytic active surfaces within the three-dimensional network, providing molecular accessibility
26 and improving the utilization of active sites.⁵² After the electrochemical oxidation step to 1.5 V_{RHE},
27 at the atomic scale most of the surface shows presence of a thin amorphous layer which is ascribed
28 to the formation of IrO_x(OH)_y species, while the core remains metallic. Shown Figure 3R is a
29 HAADF-STEM image of the IrO_x(OH)_y@NiIr structure, colored with a temperature scale to
30 highlight the intensity differences, where the blue outline corresponds to the thin (~5 Å-thick)
31 amorphous IrO_x(OH)_y layer encapsulating the core Ir-Ni solid solution phase. The presence of
32 IrO₂, very likely on the surface, and metallic Ir-Ni within the core, is supported by electron energy
33 loss spectroscopy (EELS) of NiIr-200-CL_{EO} (ESI, Figure S10) on the basis of comparison of EELS
34 measurements of IrO₂ and Ir phases from prior work.⁵³ The EELS line scan (ESI, Figure S10,C-
35 D) reveals variations in Ir O-edge intensities as well as changes in the N_{6,7}-edges ratio from the
36
37
38
39
40
41
42
43
44
45
46
47
48
49
50
51
52
53
54
55
56
57
58
59
60

1
2
3 surface to the core, which suggests changes in the electronic environment of Ir from the surface to
4
5 the core.
6

7
8 In addition to the presence of an oxide/hydroxide surface layer, a very small fraction of a
9
10 metallic surface without the presence of this amorphous layer was detected (ESI, Figure S4F). The
11
12 measurement of the lattice distances and profile intensities supports that some of the catalyst
13
14 surface is metallic after exposure to potentials of 1.5 V_{RHE} . The presence a metallic surface after
15
16 accelerated durability testing (13.5 hours at 1.6 V_{RHE}) was further supported by the presence of
17
18 CO oxidation peaks with a relative area of 15.5 ± 3.2 % of the initial CO oxidation peak area (ESI,
19
20 Figure S17). The presence of some metallic surface after the repeated exposure to high potentials
21
22 may be due to reduction of iridium oxides/hydroxides to metallic Ir during cyclic voltammetry and
23
24 CO oxidation protocols performed after the durability testing that exposed the catalyst to low
25
26 potentials of 0.05 V_{RHE} and 0.1 V_{RHE} respectively. It is also possible that metallic Ir may be
27
28 maintained by surface-level interactions, subsurface interactions, interparticle interactions, or
29
30 regions of hindered mass-transport within the nanomaterial. However, further analysis is needed
31
32 to determine the reason for the presence of a metallic Ir surface after ADT and evaluate the
33
34 conditions for reduction to iridium oxides/hydroxides to metallic Ir.
35
36
37
38
39

40 The STEM image and corresponding EDS elemental mapping (Figure 3M-P) shows that
41
42 after the electrochemical oxidation step Ir, Ni and O are well distributed within the material. The
43
44 EDS analysis supports that the initial Ni concentration of 18.8 ± 8.0 wt. % Ni for NiIr-200-CL
45
46 (ESI, Figure S2O) decreases to 6.4 ± 0.9 wt. % Ni for NiIr-200-CL_{EO} (ESI, Figure S9C) after the
47
48 electrochemical oxidation step. Post-testing analysis of the electrolyte using ICP showed that some
49
50 Ni is removed during the treatment to high potentials, as further discussed below. Prior work
51
52 supports that metallic Ni will dissolve or passivate under acidic conditions,²⁷ however as discussed
53
54
55
56
57
58
59
60

1
2
3 above previous work supports that Ni can be stabilized from dissolution in acidic conditions under
4
5 OER potentials such as within nickel-manganese antimonite⁵⁴ and Ni-Ir thin film acidic OER
6
7 catalysts that reported residual Ni values of ~12 atomic % that were likely stabilized through
8
9 interaction with Ir.⁹

10
11
12 **Oxygen Evolution Activity Measurements.** Following the electrochemical conditioning
13
14 step, the materials were electrochemically tested in the OER potential region using a rotating disc
15
16 electrode (RDE) configuration under electrode rotation of 2500 rpm in 0.1 M HClO₄ based on
17
18 previously reported methods.^{6,9,55} Shown in Figure 6A are chronoamperometric polarization
19
20 curves with the current normalized with respect to the mass of Ir of the nanoframe catalysts, NiIr-
21
22 200-CL_{EO} and NiIr-300-CL_{EO}, and commercial IrO₂-from Alfa Aesar (notated as IrO₂-AA_{EO}). As
23
24 seen from the curves, NiIr-200-CL_{EO} exhibited a significantly higher mass-normalized current than
25
26 NiIr-300-CL_{EO} or the commercial IrO₂-AA_{EO} material.

27
28
29
30
31 To ensure we were evaluating the OER activity of the catalyst within kinetic-controlled
32
33 rather than mass transfer-controlled conditions, we evaluated the effect of electrode loading and
34
35 rotation rate and determined the voltage range within the Tafel plots that exhibited a linear
36
37 response. Electrode loading has been shown to be an important factor in RDE evaluation of
38
39 oxygen reduction electrocatalysts.⁵⁶ We utilized electrode loadings of ~9-12 μg_{Ir} cm⁻²_{geo} since
40
41 higher electrode loadings were shown within our tests to result in lower mass-normalized OER
42
43 currents (ESI, Figure S11) which is attributed to mass transport phenomena related to the
44
45 accumulation of oxygen bubbles within the catalyst layer.⁶ Gas bubble dynamics and two-phase
46
47 (gas/liquid) flow were shown to significantly impact the performance and efficiency of proton
48
49 exchange membrane electrolyzer cells.⁵⁷⁻⁶⁰ Oxygen bubbles were reported to block catalyst active
50
51 sites and reduce the available catalyst ECSA,⁵⁸ and a number of factors including pore structure,
52
53
54
55
56
57
58
59
60

1
2
3 wettability, pressure and operating conditions were determined the affect oxygen bubble dynamics
4 including nucleation, growth, and detachment within the porous transport layer.⁵⁷⁻⁵⁹ Within RDE
5
6 experiments, prior work reported that at higher potentials the transport or the removal of oxygen
7
8 bubbles was a contributing factor.⁶ Within our RDE tests, we determined that changing the
9
10 rotation speed of the electrode and catalyst loading influenced the observed current in the oxygen
11
12 evolution reaction voltage range (ESI, Figure S12A-B), which we attribute to the dynamics of
13
14 oxygen formation/removal within the catalyst layer as supported by prior RDE experiments of
15
16 OER catalysts.⁶ Within the loading range of $\sim 10\text{-}30 \mu\text{g}_{\text{Ir}} \text{cm}^{-2}_{\text{geo}}$ using a rotation speed lower than
17
18 1600 rpm resulted in lower currents within the high potential range (above $\sim 1.6 \text{ V}_{\text{RHE}}$) (ESI, Figure
19
20 S12A). Using lower rotation rates (below 1600 rpm) may not allow effective removal of oxygen
21
22 bubbles from the electrode. When a higher electrode loading was used (e.g. $51 \mu\text{g}_{\text{Ir}} \text{cm}^{-2}_{\text{geo}}$), the
23
24 observed current was affected by the entire set of rotation rates tested (400-2500 rpm) (ESI, Figure
25
26 S12B), which we attribute to the higher amount of oxygen produced at the higher electrode
27
28 loadings and the effects the electrode aggregate structure on oxygen bubble dynamics.⁶ The
29
30 evaluation of the effects of loading and rotation rate informed our use of using low electrode
31
32 loadings ($\sim 9\text{-}12 \mu\text{g}_{\text{Ir}} \text{cm}^{-2}_{\text{geo}}$) and a rotation rate of 2500 rpm for evaluation of the catalyst's OER
33
34 activity.
35
36
37
38
39
40
41
42
43
44
45
46
47
48
49
50
51
52
53
54
55
56
57
58
59
60

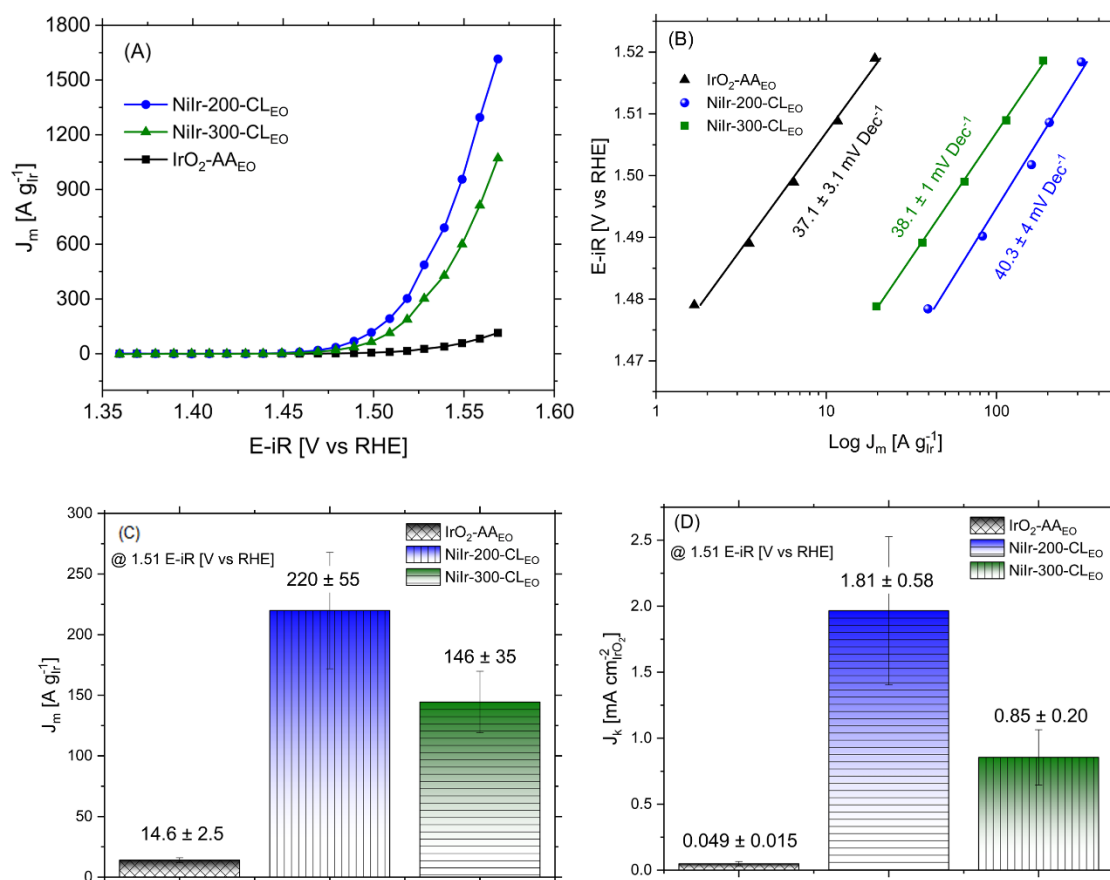


Figure 6. (A) Current in the oxygen evolution reaction (OER) voltage region determined from chronoamperometry measurements for NiIr-200-CL_{EO} ($L_{Ir}=11.7 \mu\text{g}_{Ir} \text{ cm}^{-2}_{\text{geo}}$), NiIr-300-CL_{EO} ($L_{Ir}=9.1 \mu\text{g}_{Ir} \text{ cm}^{-2}_{\text{geo}}$) and IrO_{2,EO} ($L_{Ir}=11.6 \mu\text{g}_{Ir} \text{ cm}^{-2}_{\text{geo}}$) catalysts in HClO₄ 0.1 M Ar-saturated electrolyte; increments of 10 mV and holding time of 5 s at 2500 rpm; current was normalized with respect to the mass of iridium; (B) Tafel plots obtained by chronoamperometry measurements; (C) comparison of OER mass activities for current measured at 1.51 V_{RHE}, IR-corrected; (D) comparison of OER specific activities for current measured at 1.51 V_{RHE}, IR-corrected.

Tafel plots within iR-corrected potentials between 1.47 V to 1.52 V_{RHE} were shown to provide linear Tafel slopes (Figure 6B). Since the Tafel equation is derived from the Butler-Volmer equation that describes the electrochemical reaction kinetics, the observed linear behavior in the Tafel slope supports that the reaction is primarily kinetically controlled within this voltage region.⁴ At higher potentials, deviations from linear behavior were observed (ESI, Figure S13A), and this

1
2
3 deviation is exacerbated by the increase of loading (ESI, Figure S13B). A voltage of 1.51 V_{RHE}
4 was used since the Tafel plot shows linear behavior in the 1.47 V to 1.52 V_{RHE} voltage region. The
5 current at 1.51 V_{RHE} was normalized for the Ir mass determined by ICP analysis to determine the
6 OER mass activity ($\text{A g}_{\text{Ir}}^{-1}$).
7
8
9

10
11
12
13 Using the parameters for loading, rotation speed and voltage range discussed above, we
14 determined the mass-normalized activities of the NiIr-200- CL_{EO} , Ni-Ir-300- CL_{EO} , and $\text{IrO}_{2,\text{EO}}$ at
15 1.51 V_{RHE} , as shown in Figure 6C. The NiIr-200- CL_{EO} catalyst showed significantly higher mass
16 activity than the Ni-Ir-300- CL_{EO} or the commercial $\text{IrO}_{2-\text{AA}_{\text{EO}}}$ catalyst. At a voltage of 1.51 V_{RHE} ,
17 the mass activity of NiIr-200- CL_{EO} ($220 \pm 55 \text{ A g}_{\text{Ir}}^{-1}$) was 15 times higher than the measured mass
18 activity of IrO_{2} ($14.6 \pm 2.5 \text{ A g}_{\text{Ir}}^{-1}$). We note that the OER mass activity of commercial IrO_{2} from
19 Alfa determined in this study ($14.6 \pm 2.5 \text{ A g}_{\text{Ir}}^{-1}$) is lower but in the range of the value of $22 \text{ A g}_{\text{Ir}}^{-1}$
20 which was previously reported for the same material tested under similar conditions,⁵ however
21 this latter value was obtained using linear scan voltammetry (LSV) rather than by using
22 chronoamperometry (CA) measurements. When evaluated using LSV measurements, we obtained
23 a mass activity of $19.3 \pm 3.8 \text{ A g}_{\text{Ir}}^{-1}$ for $\text{IrO}_{2-\text{AA}_{\text{EO}}}$ which is within the experimental error of the
24 previously reported value of $22 \text{ A g}_{\text{Ir}}^{-1}$.⁵
25
26
27
28
29
30
31
32
33
34
35
36
37
38
39
40

41 The significantly higher mass activity of NiIr-200-CL compared with IrO_{2} (Figure 6) may
42 be attributed to the high concentration of Ir-OH surface species and/or interaction of Ir with Ni
43 within the structure. The XPS data (Figure 4) supports the presence of NiO and Ir-OH species
44 within the surface region. From XPS data, the NiIr-200-CL sample showed a higher relative
45 concentration of NiO and Ir-OH species, and NiIr-200- CL_{EO} had a higher OER activity compared
46 with NiIr-300-CL. We note that the surface was changed after electrochemical oxidation; however,
47 the CVs after electrochemical oxidation for NiIr-200- CL_{EO} and NiIr-300- CL_{EO} (Figure 5B)
48
49
50
51
52
53
54
55
56
57
58
59
60

1
2
3 showed the presence of oxide and hydroxide species with different relative intensities and with
4 different peak voltages compared with IrO₂ which supports differences in the surface structures.
5
6
7 The presence of iridium hydroxo (Ir-OH) surface species was strongly linked to OER activity in a
8 previous study.³⁹ Leaching of nickel from the structure may contribute to the formation of highly
9 active sites based on prior work of Ir-Ni oxide thin films that suggested the leaching of nickel from
10 the structure results in highly catalytically active sites composed of Ir-OH in the vicinity of Ni.⁹
11
12
13
14
15
16
17 Recent work on yttrium-iridium catalysts also reported leaching of Y³⁺ cations into the electrolyte
18 solution resulted in the formation of a highly active IrO_x surface layer.⁶¹
19
20

21
22 Established baseline performance and testing protocols do not exist and/or are not
23 uniformly applied within the community of researchers studying acidic oxygen evolution
24 electrocatalysts.^{5-6,62} The type of electrolyte, electrochemical method (i.e. linear sweep
25 voltammetry or chronoamperometry), catalyst loading, potential of the analysis, ohmic drop
26 correction, background subtraction, etc., can influence the activity values. We therefore tested the
27
28
29
30
31
32
33 NiIr 2D nanoframe catalysts and commercial IrO₂ using identical testing protocols (Figure 6 and
34 ESI, Table S5) to directly compare the electrochemical oxygen evolution activity. To allow
35 comparison with values reported by other groups, the OER mass activities of NiIr-200-CL_{EO} and
36
37
38 Ni-Ir-300-CL_{EO} at voltages of 1.51 V_{RHE} and 1.55 V_{RHE} were compared with previously reported
39 IrNiO_x catalysts and their relevant experimental parameters in ESI, Table S6. We note that the
40
41
42
43
44
45
46
47 comparison with prior reports is affected by differences in the experimental conditions and
48 protocols used to determine the activity.

49
50 Compared with Ir-based materials reported to date that were tested under similar
51 conditions, the OER mass activity of NiIr-200-CL_{EO} (220 ± 48 A gr_{Ir}⁻¹ at 1.51 V_{RHE}) showed one
52
53
54 of the highest performance reported to date.⁵⁻⁶ Recently reported Ir-Ni nanowires showed high
55
56
57

OER mass activities of $151\text{-}810\text{ A g}_{\text{Ir}}^{-1}$ at $1.51\text{ V}_{\text{RHE}}$ at different Ir-Ni compositions.⁵ For comparison, we also determined the mass activities at $1.55\text{ V}_{\text{RHE}}$ which was used to evaluate a number of Ir-based catalysts.⁶ As discussed above, the Tafel plots of NiIr-200-CL_{EO}, Ni-Ir-300-CL_{EO}, and IrO_{2,EO} show linear behavior in the voltage region of $1.47\text{-}1.52\text{ V}_{\text{RHE}}$, but deviate from linear behavior above $\sim 1.52\text{ V}_{\text{RHE}}$ (ESI, Figure S13A) which supports that the current at 1.55 V may be affected by mass-transport processes and not only controlled by the reaction kinetics. The measured OER mass activity of iridium oxide (IrO₂-Alfa) from our tests ($90 \pm 26\text{ A g}_{\text{Ir}}^{-1}$ at $1.55\text{ V}_{\text{RHE}}$) was somewhat lower than the previously reported value of $140\text{ A g}_{\text{Ir}}^{-1}$ at $1.55\text{ V}_{\text{RHE}}$ for the same commercial material;¹³ however, this difference is attributed to the experimental analysis method, as explained above. Using the current from LSV measurements, the mass activity of IrO_{2,EO} was $131 \pm 13\text{ A g}_{\text{Ir}}^{-1}$, in agreement with the previous report for this material.¹³ In general, the data obtained using LSV showed higher activities in comparison with those obtained by chronoamperometry, for example at $1.51\text{ V}_{\text{RHE}}$, 307 ± 80 and $213 \pm 17\text{ A g}_{\text{Ir}}^{-1}$ were obtained for NiIr-200CL_{EO} and NiIr-300CL_{EO} respectively. The apparently higher activities obtained from LSV measurements are an artifact of the additional contribution of current due to capacitance which is included in the LSV measurements, and the contribution of capacitive current can be even higher for supported materials. We consider that quasi-steady-state current obtained from chronoamperometry measurements is more reliable for determining OER current, as also supported by other's analysis.² Carbon-supported Ir-Ni bimetallic nanoparticles showed a higher activity of ($498\text{ A g}_{\text{Ir}}^{-1}$ at $1.51\text{ V}_{\text{RHE}}$)¹³ compared with NiIr-200CL_{EO} ($220 \pm 48\text{ A g}_{\text{Ir}}^{-1}$ at $1.51\text{ V}_{\text{RHE}}$), however the contributions of capacitance and carbon corrosion to the current value were not considered in the analysis. For Ir-Ni bimetallic nanoparticles, the corrosion process was evident

1
2
3 after 12 hours where the voltage significantly increased which indicates the catalyst is not stable
4
5 over extended periods.¹³
6

7
8 In addition to the OER mass activities, the OER current was also normalized to the IrO₂
9
10 electrochemical surface area (ECSA_{IrO₂}) determined from pseudocapacitance measurements, as
11
12 described above. As shown in Figure 6D, the OER specific activities at 1.51 V_{RHE} of 1.81 ± 0.58
13
14 A cm_{IrO₂}⁻² for NiIr-200-CL_{EO} and 0.85 ± 0.20 A cm_{IrO₂}⁻² for Ni-Ir-300-CL_{EO} are significantly higher
15
16 than the OER specific activity of 0.049 ± 0.015 A cm_{IrO₂}⁻² for commercial IrO₂ (IrO₂-AA_{EO}). In
17
18 addition, we evaluate the specific activities at 1.55 V_{RHE} for comparison with OER specific activity
19
20 values reported by others. The OER specific activities at 1.55 V_{RHE} of 11.5 ± 4.2 A cm_{IrO₂}⁻² for
21
22 NiIr-200-CL_{EO} and 4.50 ± 0.88 A cm_{IrO₂}⁻² for Ni-Ir-300-CL_{EO} are substantially higher than the
23
24 values of number of Ir and IrO₂ catalysts tested under similar conditions (0.48 - 1.00 A cm_{Ir}⁻²)⁶ and
25
26 are within the range of specific activities of IrNi and IrCo nanowire OER catalysts (\sim 5 - 7 A cm_{Ir}⁻²)⁵ however, the values are not directly comparable since these previously reported values were
27
28 determined using ECSA_{Ir} rather than ECSA_{IrO₂} as used within this study.
29
30
31
32
33
34
35
36

37
38 The Tafel slope measures the dependency of the ohmic-drop corrected overpotential on the
39
40 current density and provides useful information on the reaction mechanism.^{2,4} The Tafel slopes of
41
42 NiIr-200-CL_{EO} (40.3 ± 4 mV dec⁻¹) and Ni-Ir-300-CL_{EO} (38.1 ± 1 mV dec⁻¹) are similar to the
43
44 Tafel slopes as IrO₂-AA_{EO} (37 ± 3.1 mV dec⁻¹) within the range of experimental error of the
45
46 measurements, suggesting similar reaction mechanisms. The acidic oxygen evolution reaction
47
48 involves a complicated reaction mechanism with multiple intermediates, with the “electrochemical
49
50 oxide path” involving two proton-electron transfer steps followed by an oxygen recombination
51
52 step.³ A theoretical analysis of Tafel slopes determined a Tafel slope of 120 mV dec⁻¹ for the first
53
54
55
56
57

1
2
3 electron transfer step being rate determining, whereas a Tafel slope of 40 mV dec^{-1} corresponds to
4
5 the second electron transfer step being rate determining.⁶³ Based on this analysis, the measured
6
7 Tafel slopes of NiIr-200-CL_{EO} ($40.3 \pm 4 \text{ mV dec}^{-1}$) and Ni-Ir-300-CL_{EO} ($38.1 \pm 1 \text{ mV dec}^{-1}$) are
8
9 consistent with the second electron transfer step as the rate determining step; however microkinetic
10
11 analysis has demonstrated that changes of the coverage of adsorbed species, which was not
12
13 considered here, may alter Tafel slopes.⁶⁴ The measured Tafel slope of IrO₂ from this study ($37 \pm$
14
15 3.1 mV dec^{-1}) is similar to some previously measured values for IrO_x (34 mV dec^{-1}),⁵⁵ however
16
17 other studies reported higher Tafel slopes of $\sim 60 \text{ mV dec}^{-1}$ for IrO₂⁴ that were determined from
18
19 currents obtained from chronoamperometry measurements. We found significant differences
20
21 between Tafel slopes determined from currents measured using chronoamperometry and LSV,
22
23 with higher Tafel slopes using currents obtained LSV. These differences can be related to the
24
25 experimental considerations described above.
26
27
28
29
30

31 **Computational Model and Results.** Experimental observations show the formation of a
32
33 thin amorphous surface layer over the catalyst after electrochemical oxidation and the presence of
34
35 surface oxides, hydroxides, and nickel within the surface region. The exact atomic-level structure
36
37 of the surface and the thin amorphous layer and the distribution of the dopant with respect to the
38
39 oxide phase are not known yet from the current study. Here, first principles calculations were used
40
41 to investigate the effect of Ni substitution on the surface layer and obtain insights on the effect of
42
43 Ni substitution within representative model surface structures. Thus, in order to investigate the role
44
45 of Ni on the OER reaction mechanism, we adopted a computational approach in which Ni is within
46
47 the surface level, so that its contribution to the OER is maximized. Our catalyst model consists of
48
49 a rutile (110) crystalline facet of IrO₂. The pristine (110) surface is formed by four iridium atoms:
50
51 two penta-coordinated (5Ir) and two hexa-coordinated (6Ir) (ESI, Table S7). The surface also
52
53
54
55
56
57

contains two types of oxygen atoms: bridge (O_b) and three-coordinated (O_t) oxygen atoms, which are located above and on the plane of the metal atoms, respectively, as shown in Figure 7A,B. To consider the presence of Ni at the surface, one metallic site (25% of the surface layer) was substituted by Ni (110). Two Ni-doped structures were considered to represent the different regions of the electrocatalyst: doping a 5-coordinated ($5Ni-IrO_2$) or a 6-coordinated ($6Ni-IrO_2$) site, as represented in Figure 7c and d respectively. Although it is noteworthy that the modeled structures do not exactly represent the experimental scenario, they are still very useful to provide insights on the role of Ni on the overall OER mechanism.

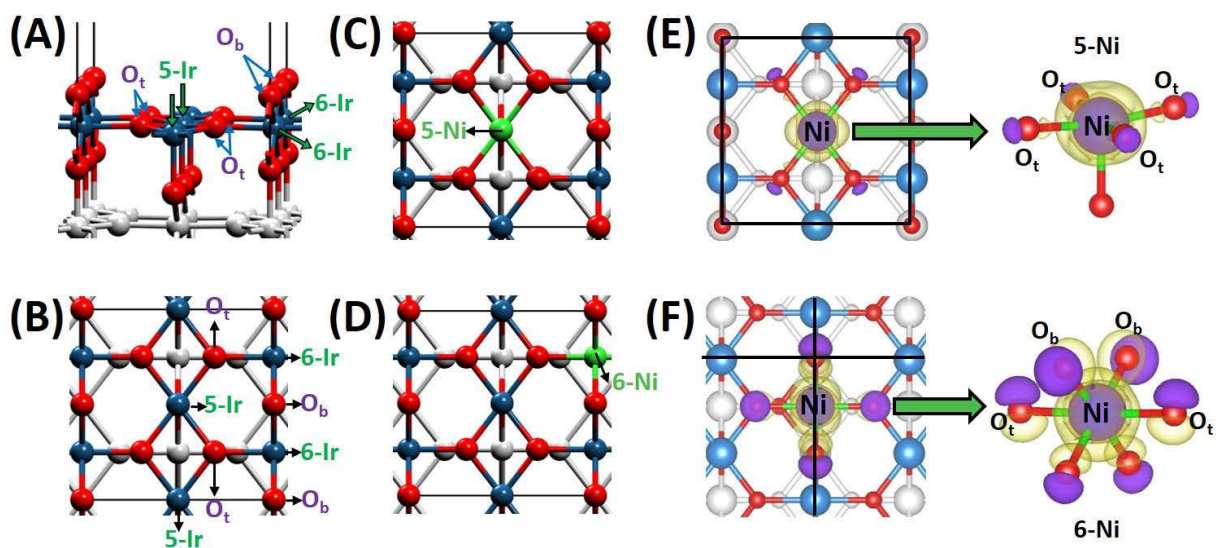
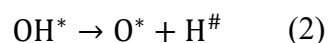


Figure 7. Electro-catalyst model: (a) lateral and (b) top view of the (110)- IrO_2 model slab; top-view of Ni-doping at (c) 5-fold ($5Ni-IrO_2$) and (d) 6-fold ($6Ni-IrO_2$) coordination sites; electronic density accumulation (purple)/depletion (yellow) on the surface plane of (e) $5Ni-IrO_2$ and (f) $6Ni-IrO_2$ structures. Surface layer color code: O, red; Ir, blue; Ni, green. Black lines depict the edges of the simulation cell. Subsurface atoms are shown in white.

It is expected that the presence of the dopant atom alters the electronic environment of the doping site. Electronic density difference graphs were calculated as the change in the electronic charge density of the doped systems and the pure system, as shown in Figure 7e and f. In both

1
2
3 cases (5Ni- and 6Ni-IrO₂), nickel exhibited accumulation (purple) of electron density, yielding
4
5 electron density depletion (yellow) between the Ni and neighboring oxygen atoms. Table S7 (ESI)
6
7 shows the calculated Bader charges for four metallic atoms representing the (110) lattice surface
8
9 of pristine IrO₂, and IrO₂ with Ni-substituted in 5-coordinated and 6-coordinated sites (i.e. 5Ni-
10
11 IrO₂, and 6Ni-IrO₂). For the pristine IrO₂, the charge of the 6-fold coordinated Ir atoms (1.70 |e|)
12
13 is higher than the 5-fold coordinated ones (1.50 |e|). When the surface is doped, Ni charges are less
14
15 positive (1.22-1.32 |e|) reflecting electron density accumulation around the doped site. It is
16
17 remarkable that the presence of Ni in the hexa-coordinated site leads to strong accumulation of
18
19 electron charge density within the bridging oxygen atoms (O_b), see Figure 7f. However, if the Ni
20
21 is in the 5-Ni site, the electron charge density change is negligible on the surrounding O_t atoms
22
23 (Figure 7e). This result is very important since it has been found that the O_b atoms can serve as
24
25 proton donor-acceptor during the OER.^{3,10,65-66} Overall, the change in the chemical environment
26
27 of the surface active sites due to the Ni dopant is expected to affect the catalytic OER activity of
28
29 the anode.
30
31
32
33
34

35
36 The electrochemical oxide path or direct O₂ recombination mechanism has been commonly
37
38 proposed as the water splitting reaction pathway for the OER on the anode.^{3,8,63,67} In this work we
39
40 adopted such a mechanism and studied the adsorption of the different intermediates of reaction
41
42 (H₂O, OH, and O) followed by their reactions on our catalyst model surfaces. Here we considered
43
44 the following three surface reactions: first and second oxidation stages of water (eq. 1 and 2) and
45
46 recombination of atomic oxygen atoms (eq. 3).
47
48



1
2
3 where X^* (e.g. H_2O^* , OH^* or O_2^*) represents the X species adsorbed on an active metal site (Ir or
4 Ni) and $H^\#$ is a hydrogen attached to a bridge-oxygen atom O_b . Bridging oxygen atoms have
5
6 already been considered an important part of the OER as a proton acceptors.^{8,10} Here we consider
7
8 not only a thermodynamic approach, but also kinetic barriers in order to provide a more
9
10 comprehensive understanding of the effect of Ni on the activity of the IrO_2 surface. We note that
11
12 following the surface reactions, the overall mechanism involves subsequent electron transfer and
13
14 proton formation (1st and 2nd oxidation stages) and oxygen desorption steps, as represented by the
15
16 3 arrows in Figure 8. The energies involved in these desorption steps were not specifically
17
18 included within the current computations, and it is possible that the energies involved in these steps
19
20 may influence the overall reaction pathway. Further work may include a relative different model
21
22 to include the interaction of the species being desorbed with the medium.
23
24
25
26
27

28 The adsorption of water on the oxide surface was tested on all non-equivalent metallic sites.
29
30 For the pristine system, although the surface has four metallic sites, there are only two that are
31
32 different, i.e., one 5-Ir (Ir with coordination five) and one 6-Ir (Ir with coordination six). In the
33
34 case of Ni-doped in the 5-fold coordinated site (5Ni- IrO_2 system, see Figure 7c), there are two
35
36 non-equivalent 5-coordinated sites (5-Ni and 5-Ir) and one 6-Ir site. Finally, for the 6Ni- IrO_2 slab,
37
38 there are again one 5-Ir and two 6-coordinated sites (6-Ni and 6-Ir). Adsorption energies are
39
40 reported in ESI, Table S8. In general, it is found that the adsorption on penta-coordinated metallic
41
42 sites is significantly stronger (<-0.42 eV) than on the hexa-coordinated sites (>-0.11 eV).
43
44 Therefore, it is more likely for the water to adsorb on 5-Ir and 5-Ni rather than on hexa-coordinated
45
46 sites. In addition, the optimized structures (ESI, Figure S14) also reveal that the water interaction
47
48 energy on 6-Ni and 6-Ir sites is due to hydrogen bonds between the water hydrogen atoms and the
49
50 bridge oxygen atoms (O_b) from the surface, in contrast to the water adsorption on 5-Ir and 5-Ni
51
52
53
54
55
56
57

1
2
3 site in which actual adsorption ($\text{H}_2\text{O}-\text{M}$) is observed. This is in good agreement with previously
4 reported studies of water adsorption on metal oxides, where it was found that water prefers to
5 adsorb on the 5-coordinated metallic sites.^{8,68} It has also been reported that these sites are expected
6 to constitute the active center for the OER.^{3,10,66,69} For that reason, only 5-Ni and 5-Ir sites were
7 considered for the remaining part of the analysis.
8
9

10
11
12
13
14
15 The adsorption energies of H_2O , OH, and O on 5-coordinated sites for the three surface
16 slabs are summarized in ESI, Figure S15. Overall, it is found that the adsorption energies remain
17 almost unchanged when any of the species is attached to the Ir sites regardless of surface doping.
18 However, when the adsorption occurs on the 5-Ni site, the adsorption energies are lowered by up
19 to 60%. For instance, the adsorption of water is lowered by nearly 60 % compared to the pristine
20 IrO_2 surface (-1.02 eV)⁸ if it occurs on the 5-Ni site (-0.42 eV). However, if the adsorption happens
21 on the undoped site, the adsorption energy (-0.98 eV) is comparable to the undoped case and very
22 similar to systems with Ni occupying the 6-fold coordination site (-0.95 eV). The adsorption
23 energy of OH and O on 5-Ni sites are -1.64 and -2.21 eV, respectively, which represents 46 and
24 48% lower energies with respect to adsorptions on Ir sites (5-Ir) either on pristine or doped IrO_2
25 surfaces. The main impact of this adsorption behavior might be for adsorbed species that may
26 recombine on adjacent active sites. For example, the recombination of oxygen atoms might be
27 enhanced if one of the oxygen atoms is more weakly adsorbed than the other.
28
29
30
31
32
33
34
35
36
37
38
39
40
41
42
43
44
45
46
47
48
49
50
51
52
53
54
55
56
57
58
59
60

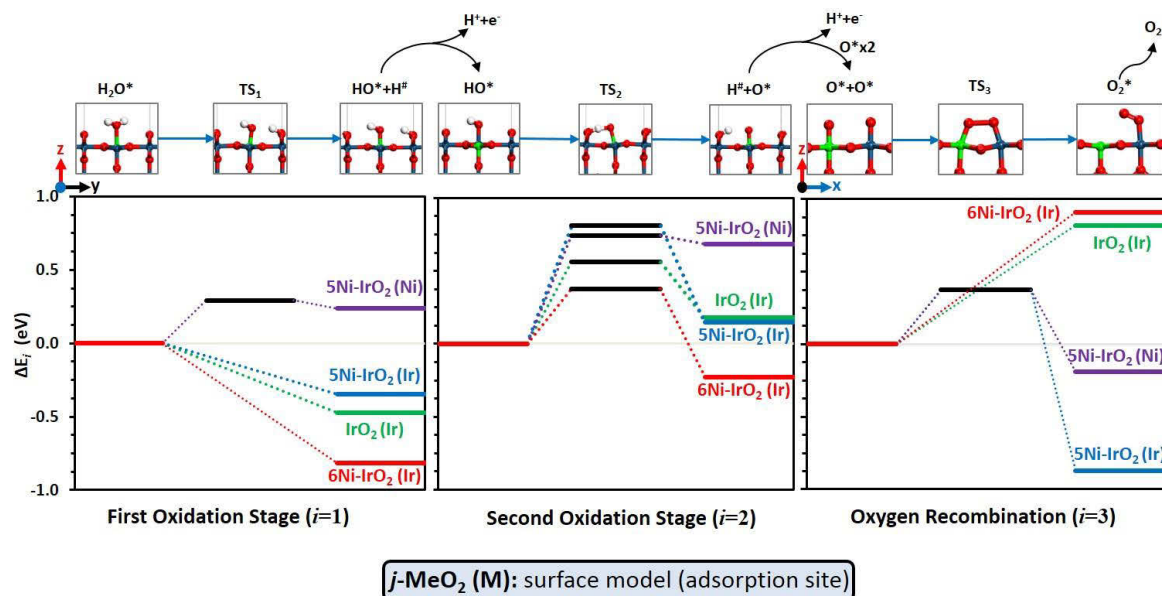


Figure 8. Reaction and activation energies for first and second oxidation stage (O-H bond breaking) and oxygen recombination on the pristine⁸ and Ni-doped IrO₂. In the case of 5D-IrO₂ (M), two curves are shown depending on the adsorption site M (Ni or Ir). Black-line markers indicate transition states (TS_{*i*}) energies – activation barriers. Top panels color code: O, red; H, white; Ni, green.

Figure 8 shows the reaction energies, activation barriers (transition states), and a representative model (top panels) for the three steps of the OER described in eq. 1 to 3. The first oxidation stage ($i=1$) is characterized by the first O-H breaking; the resulting proton (H) will attach to one of the closest neighbor O_b atoms. The larger this downhill step is, the more thermodynamically favorable the reaction is. Therefore, the presence of Ni in the 6-coordinated site (6Ni-IrO₂ (Ir)) enhanced the reaction energy (ΔE_1) from -0.47 to -0.82 eV with respect to the pristine IrO₂, making the first oxidation stage more favorable. On the other hand, when the surface is doped in the penta-coordinated site and the adsorption of water was initially on the Ir site, the energy of reaction is slightly higher (-0.35 eV) than the undoped system, but still favorable. In contrast, a small positive reaction energy (0.24 eV) is observed for the first O-H breaking when the water seats on the Ni-doped site. Regarding the kinetics, no activation barrier is observed for

1
2
3 the 6Ni-IrO₂ (Ir) and 5Ni-IrO₂ (Ir) systems, similar to what has been reported for pure and Co-
4 doped IrO₂ and RuO₂ systems.⁸ Nevertheless, when the water adsorbs on the Ni-doped 5-
5 coordinated site, a 0.29 eV activation barrier is predicted. In summary, the easiness in which the
6 first oxidation step can occur follows this trend: 6Ni-IrO₂ (Ir) > IrO₂ (Ir) > 5Ni-IrO₂ (Ir) > 5Ni-
7 IrO₂ (Ni).

8
9
10
11
12
13
14
15 The second oxidation stage ($i=2$) is described by the O-H splitting of an adsorbed OH. The
16 graph (Figure 8) shows that for pure and 5-coordinated Ni-doped IrO₂ systems (IrO₂ and both 5Ni-
17 IrO₂), this step is uphill which means that the second oxidation stage is predicted to be
18 endothermic, $\Delta E_2 > 0$. Interestingly, when the reaction occurs in the 6Ni-IrO₂ system, the reaction
19 is exothermic ($\Delta E_2 = -0.23$ eV), which shows a significant improvement in OER compared to the
20 pure IrO₂ surface ($\Delta E_2 = 0.18$ eV). Regarding the 5Ni-IrO₂ system, the reaction energy (0.15 eV) is
21 just slightly lower than the undoped case when the OH was initially adsorbed on the Ir site and
22 higher ($\Delta E_2 = 0.68$ eV) when OH breaks on the Ni site. The activation energies for the second O-H
23 bond breaking are shown in Figure 8 (TS₂[#]), and the following trend is obtained: 6Ni-IrO₂ (0.38
24 eV) < IrO₂ (0.56 eV) < 5Ni-IrO₂ (0.74 or 0.81 eV). According to the calculated kinetic barriers,
25 the second O-H breaking seems to be more determinant in the OER compared to the first O-H
26 breaking, which exhibits very low or null activation energies. The higher activation energies
27 calculated for the second step would indicate that the second step is rate-determining, which is
28 consistent with the experimental Tafel slopes determined for NiIr-200-CL_{EO} and Ni-Ir-300-CL_{EO},
29 discussed above, that support that the second electron transfer step is the rate determining step.

30
31
32
33
34
35
36
37
38
39
40
41
42
43
44
45
46
47
48
49 Remarkably, the changes in the electronic charge density due to the presence of Ni bonding
50 the bridge oxygen atoms (O_b), i.e., in 6-fold coordinated sites significantly enhance the activity of
51 the O_b towards accepting the proton from the OH leading to a decrease of around 30% the
52
53
54
55
56
57
58
59
60

1
2
3 activation energy compared to the pristine surface. Some would expect that the activation energy
4
5 to be correlated with the reaction energy; however, for the 5Ni-IrO₂ system, the activation energy
6
7 for the OH oxidation on Ni sites is lower than the case when it is adsorbed on the Ir case, a trend
8
9 that is contrary to one for the reaction energies. Therefore, although the reaction energies are very
10
11 valuable and can give overall pictures of the mechanism, this example shows that it is very
12
13 important to evaluate both thermodynamics and kinetics of the reactions.
14
15
16

17 To summarize the results involving hydrogen transfer (eq. 1 and 2), it is found that Ni
18
19 doping in the 6-coordinated site enhanced not only the thermodynamics, but also the kinetic
20
21 behavior of the OER compared to the pristine electrocatalyst as seen in Figure 7 (left and middle).
22
23 The main reason of the improvement is that the Ni changes the chemical environment of the O_b
24
25 atoms (see Figure 7f) that act as proton acceptors during the reaction. Regarding the last step –
26
27 oxygen recombination (eq. 3), we assume that another molecule of water has to undergo the same
28
29 steps described by eq. 1 and 2 on an adjacent site to the already formed O species. Another scenario
30
31 might be the case where two water molecules oxidize simultaneously to form two O atoms
32
33 adsorbed in adjacent sites. In any case, both water molecules have to go through the reactions in
34
35 eq. 1 and 2, and the presence of the adjacent species may have a minimal effect on the reactions
36
37 and activation energies. Therefore, Figure 8 (*i*=3) shows the oxygen recombination step from two
38
39 adjacent 5-coordinated sites. It is found that the formation of molecular oxygen is endothermic for
40
41 pure and 6Ni-IrO₂ systems ($\Delta E_3 > 0.80$ eV) with no additional activation energy. However, when
42
43 Ni acts as a dopant in the 5-coordinated site, this reaction step becomes exothermic ($\Delta E_3 < 0$) with
44
45 small activation energies (~0.37 eV). This corroborates our initial hypothesis that the different
46
47 strength of adsorption of two adjacent sites could be beneficial for recombination reactions. Based
48
49 on this analysis, we can infer that the presence of Ni in a 6-coordinated site favors any reaction
50
51
52
53
54
55
56
57
58
59
60

1
2
3 involving proton transfer, i.e., the oxidation stages, whereas the Ni doping in the adsorption sites
4 (five-fold coordinated) lowers the activation barriers and energy of reaction for the oxygen
5 recombination. Therefore, the existence of Ni at the surface layer can improve the activity of the
6 electrocatalysts towards some steps of OER, with the beneficial effect depending on the location
7 of the dopant. In addition, we might expect to have some synergistic effects if the Ni is present in
8 both types of sites. In this case, it might be possible to obtain a combined effect that improves the
9 overall OER. Additional details on the mechanism and effect of doping on the activity of IrO₂ will
10 be discussed elsewhere.

21 **Evaluation of Electrocatalyst Stability.** Following our experimental and theoretical
22 analysis of the OER activities of the catalysts, we evaluated the catalyst stability. Catalyst stability
23 is a particularly important parameter to determine for development of PEM electrolyzers,^{1,70} and
24 catalyst degradation will affect PEM electrolyzer performance particularly at low catalyst
25 loadings.⁵ For testing catalyst stability, an accelerated durability test (ADT) using a constant
26 potential of 1.6 V for 13.5 hours was used. This protocol had been previously utilized to evaluate
27 the durability of a number of iridium-based catalysts.⁵⁻⁶ Prior work supported these durability
28 conditions within RDE tests yielded similar losses as in electrolyzers with low anode loadings,⁶
29 however losses with RDE cells occurred at lower potentials and at a shorter timeframe.⁵ Shown in
30 Figure 9A,B is the comparison of the current obtained from chronoamperometric measurements
31 in the OER region and Tafel plots of IrO_{2,EO}, NiIr-200-CL_{EO}, and Ni-Ir-300-CL_{EO} before and after
32 the ADT protocol respectively. A summary of the OER mass activities at 1.51 V_{RHE} before and
33 after ADT are presented in Figure 9C, and details are presented in Table S6. The IrO₂ samples
34 showed relative percent retention of 71 ± 7 % of the initial mass-normalized current after ADT.
35 Both the NiIr-200-CL_{EO} and NiIr-300-CL_{EO} catalysts exhibited a relative stability of 42 ± 26 %
36
37
38
39
40
41
42
43
44
45
46
47
48
49
50
51
52
53
54
55
56
57
58
59
60

1
2
3 and 24 ± 11 % respectively, indicating a lower relative stability compared with IrO₂. We also
4
5 compared the OER specific activities before and after ADT. Similar stability trends were observed
6
7 for OER specific activity compared with OER mass activity. The OER specific activities of NiIr-
8
9 200-CL_{EO} and Ni-Ir-300-CL_{EO} significantly decreased after ADT, but the OER specific activities
10
11 remained higher than IrO₂ after ADT (Figure 9D). The relatively high estimated standard deviation
12
13 of the OER activity values is attributed to differences in the electrode layers for the self-supported
14
15 catalysts. A prior study has identified that blocking of the catalyst surface by evolved gas bubbles
16
17 and detachment of the catalyst from the electrode surface may lead to a decrease of the catalyst
18
19 active surface area being exposed to the electrolyte.⁷¹
20
21
22
23
24
25
26
27
28
29
30
31
32
33
34
35
36
37
38
39
40
41
42
43
44
45
46
47
48
49
50
51
52
53
54
55
56
57
58
59
60

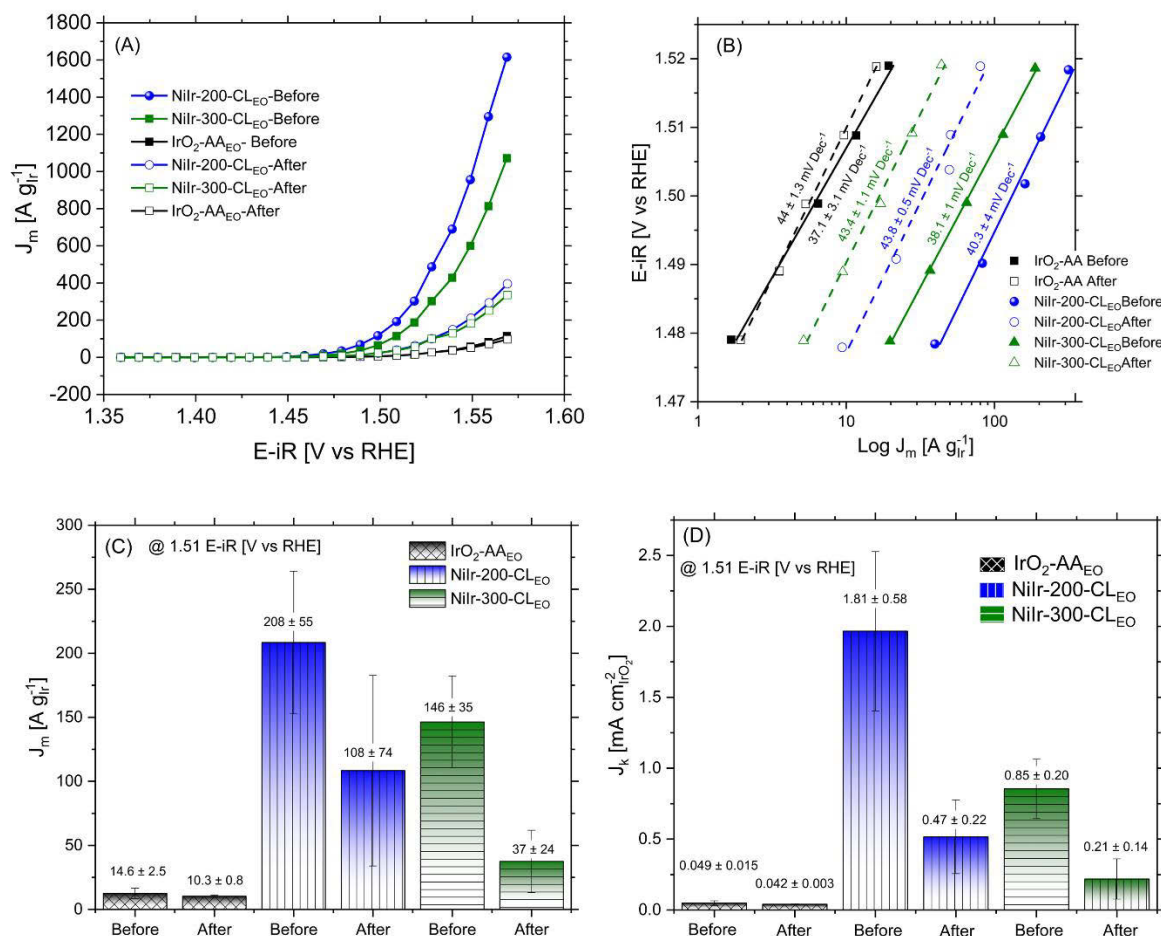


Figure 9. Representative electrochemical performance of Ni-Ir 2D nanoframes (NiIr-200-CL and NiIr-300-CL) and commercial IrO₂ before and accelerated durability testing (ADT) in O₂-free 0.1 M HClO₄ using electrode loadings of $L_{Ir}=11.7 \mu\text{g}_{Ir} \text{cm}^{-2}_{\text{geo}}$ (NiIr-200-CL_{EO}), $L_{Ir}=9.1 \mu\text{g}_{Ir} \text{cm}^{-2}_{\text{geo}}$ (NiIr-300-CL_{EO}) and $L_{Ir}=11.6 \mu\text{g}_{Ir} \text{cm}^{-2}_{\text{geo}}$ (IrO₂-AA_{EO}); the stability was carried out using a potentiostatic procedure by holding the working electrode at 1.6 V_{RHE}-iR-corrected for 13.5 hours under rotation at 2500 rpm. (A) Current in the oxygen evolution reaction (OER) voltage region before and after ADT determined from chronoamperometry measurements; (B) Tafel slopes before and after ADT determined by chronoamperometry; (C) comparison of OER mass activities at 1.51 V_{RHE} before and after ADT; (D) comparison of OER specific activities at 1.51 V_{RHE} before and after ADT.

From our tests, the Tafel slopes of NiIr-200-CL_{EO} and NiIr-300-CL_{EO} catalysts remained similar before and after the durability testing whereas the Tafel slope of IrO₂ slightly increased above the estimated standard deviation (Figure 9B). Prior testing of the durability of iridium-nickel

1
2
3 nanowires showed that the composition affected both the activity and durability.⁵ While Ir-Ni
4
5 nanowire catalysts with lower activities showed high durabilities (85-90 %), catalysts with the
6
7 highest activities also showed durabilities of ~10-33% of initial activity using a similar ADT
8
9 conditions,⁵ which is in a similar range as the catalysts reported here. We also note that within this
10
11 prior study a voltage of 1.55 V was to evaluate the OER mass activities, which is different than
12
13 the voltage of 1.51 V_{RHE} reported here.
14
15

16
17 Although the relative stability of NiIr-200-CL_{EO} was lower than IrO_{2,EO}, the OER mass
18
19 activity remains significantly higher than IrO₂ (Figure 9C) even after durability testing. In addition,
20
21 the OER mass activity of NiIr-200-CL_{EO} after ADT of $108 \pm 74 \text{ A g}_{\text{Ir}}^{-1}$ at 1.51 V_{RHE} remains higher
22
23 than $\sim 25 \text{ A g}_{\text{Ir}}^{-1}$ at 1.51 V_{RHE} for ATO-IrNiO_x after ADT,⁷² although we note the significant error
24
25 range of the value and that different stability testing protocols and electrolyte solution were used,
26
27 so a direct comparison is not possible. For comparison with testing protocols used by other groups
28
29 for evaluating OER activity and stability,⁷² the mass activity of the NiIr-200CL_{EO} catalyst was also
30
31 evaluated using 0.05 M H₂SO₄ and using a stability test that consisted of applying a constant
32
33 current density of 1 mA cm⁻² for 15 hours (ESI, Figure S18 and Table S9). Using these conditions,
34
35 the NiIr-200CL_{EO} catalyst still presented higher activity and lower stability relative to IrO₂.
36
37
38
39

40
41 Based on the observed degradation over the accelerated durability test, we determined the
42
43 percent Ir and Ni within the structure after the ADT using EDS mapping and analyzed Ir and Ni
44
45 dissolution within the electrolyte. EDS mapping of NiIr-200-CL after the accelerated durability
46
47 test (ESI, Figure S9,E-O) showed that after repeated cycling to 1.8 V_{RHE} during the OER
48
49 measurements and after the accelerated durability test of 13.5 h at 1.6 V_{RHE}, nickel was still present
50
51 within the material at a similar level as before the ADT measurements (ESI, Figure S9,A-D). To
52
53 determine the contribution of Ir and Ni dissolution to the catalyst degradation, analysis of the
54
55
56
57
58
59
60

1
2
3 amount of Ir and Ni dissolved within the electrolyte during the accelerated durability test was
4 performed using ICP-MS. Prior work supports that Ir dissolution occurs during OER potentials,⁷³
5 and Ir dissolution is highly dependent on the applied potential.⁴⁰ Quantitative analysis of the
6 electrolyte solution after accelerated durability testing using ex-situ ICP measurements showed
7 only 1.5 ± 0.1 % of Ir in solution for IrO_{2,EO}, while 13.3 ± 0.1 % was found for NiIr-200CL_{EO} (ESI,
8 Table S9). The higher dissolution of Ir for the Ni-containing materials is consistent with a previous
9 study that reported ~34-47 times higher Ir dissolution rate for Ir-Ni oxide films compared with
10 IrO_x.⁹ Comparison of the percent Ir dissolution with the percent OER mass activity loss after
11 ADT supports that the loss in the OER activity is not entirely due to Ir dissolution but also
12 diminishing of electroactive surface area due to agglomeration and/or changing the nature of active
13 catalytic sites (i.e. due to Ni depletion). The change of the catalyst surface after ADT is supported
14 by the disappearance of the peak ~0.4 V within the CVs of the NiIr-200CL_{EO} and NiIr-300CL_{EO}
15 catalysts after ADT (ESI, Figure S16), since the peak at ~0.4 V has been associated to the presence
16 of iridium oxy/hydroxy species and improving of the activity.

17
18
19 We further analyzed the rate of dissolution before and after ADT by analysis of the
20 electrolyte solution using ICP and integrating the experiment time. The Ir corrosion rate within
21 the NiIr-200CL_{EO} catalyst was significantly different before and after ADT and was also
22 determined to be correlated with the leaching of Ni. The NiIr-200-CL_{EO} catalyst before the ADT
23 measurements showed an Ir dissolution rate of 308 ± 46 pg_{Ir} cm⁻²s⁻¹ and a Ni dissolution rate of
24 710 ± 50 pg_{Ni} cm⁻²s⁻¹. However, the dissolution rates drastically decreased after ADT to an Ir
25 dissolution rate of 35.5 ± 1.2 pg_{Ir} cm⁻²s⁻¹ and a Ni dissolution rate of 29.8 ± 3 pg_{Ni} cm⁻²s⁻¹. The
26 reduction of Ir dissolution with time may be related with the depletion of Ni near to the surface
27 and formation of a IrO₂ passivating layer as observed by STEM. Similar behavior has been
28
29
30
31
32
33
34
35
36
37
38
39
40
41
42
43
44
45
46
47
48
49
50
51
52
53
54
55
56
57
58
59
60

1
2
3 reported for $\text{Ir}_x\text{Os}_{1-x}$ alloys.⁷⁴ During dealloying at 1 mA cm^{-2} , fast dissolution of Os and Ir were
4
5 registered during the first 1000 s, followed by a decrease of dissolution rate at longer times, and
6
7 the total percent of dissolution of iridium was markedly governed by the amount of Os within the
8
9 samples.
10

11 12 13 14 **3. Conclusions**

15
16 Self-supported hydrous iridium-nickel oxide 2D nanoframes exhibit a unique catalytic
17
18 nanoarchitecture that results in dramatically higher OER electrocatalytic activity compared with
19
20 IrO_2 and other Ir-based OER electrocatalysts. The hierarchical iridium-nickel oxide/hydroxide 2D
21
22 nanoframe architecture is formed through temperature/atmosphere treatment of Ir-decorated NiO
23
24 nanosheets followed by chemical leaching. After chemical leaching, a metallic Ir-Ni alloy phase
25
26 with oxides and hydroxides at the surface region was formed. The thermally treated and chemically
27
28 leached sample retained a 2D framework structure consisting of interconnected nanocrystallites
29
30 and through-connected porosity allowing 3D molecular accessibility. Electrochemical cycling to
31
32 high potentials ($1.5 \text{ V}_{\text{RHE}}$) resulted in the formation of a $\sim 5 \text{ \AA}$ thick surface oxide/hydroxide layer.
33
34
35

36
37 The NiIr-200-CL catalyst showed more than an order of magnitude (15 times) higher mass
38
39 activity compared with commercial IrO_2 and higher activities compared with numerous other Ir-
40
41 based OER catalysts. The significantly higher mass activity and specific activity of NiIr-200-CL
42
43 compared with IrO_2 may be attributed to specific nature and concentration of Ir-OH surface species
44
45 and/or interaction of Ir with Ni within the surface region. From analysis of the experimental and
46
47 theoretical Tafel slopes and our computational analysis, the second electron transfer step was
48
49 determined to be the rate determining step for the reaction. Density functional theory calculations
50
51 support that Ni substituted within IrO_2 lowers the activation energy for adsorbed intermediates of
52
53 second electron transfer step of the OER reaction. The effect of the dopant on bridging sites also
54
55
56
57

1
2
3 emphasizes the importance of considering the OER reaction not as a single site reaction but as
4 involving multiple sites along the reaction pathway. Adjusting interactions for the multiple sites
5 involved in the reaction steps provides a pathway to develop improved OER catalysts that move
6 beyond the typical volcano plot trend that describes activity with a single descriptor.^{10,64}
7
8
9
10
11

12
13 The thermal reduction treatment temperature was determined to significantly affect the
14 electrocatalyst surface structure, OER activity, and stability. X-ray photoelectron spectroscopy
15 analysis showed that the sample heated to 200 °C showed a higher relative surface concentration
16 of hydrous IrO₂ and nickel oxide, while heating to 300 °C resulted in a higher relative concentration
17 of anhydrous IrO₂ and lower relative concentration of NiO within the surface region. After
18 electrochemical oxidation, the CVs of the NiIr 2D nanoframes heated to 200 °C and 300 °C showed
19 the presence of surface oxide and hydroxides with different relative peak areas depending on the
20 treatment temperature and with different relative peak positions compared with IrO₂ which
21 supports differences in the surface structures between the catalysts. The different surface structures
22 significantly affect the OER activity with the sample heated to 200 °C showing higher OER activity
23 than heating to 300 °C. The higher OER activity obtained using a lower temperature treatment
24 underlies the importance of using thermal treatment temperatures and processing conditions that
25 result in the presence of surface hydroxides and maintain non-noble metals within the surface
26 region can result in improved activity OER electrocatalysts.
27
28
29
30
31
32
33
34
35
36
37
38
39
40
41
42
43
44
45

46 This work demonstrates the ability to make an integrated metal alloy nanostructure which
47 can be chemically leached and then electrochemically conditioned to form an oxygen evolution
48 with very high activity and stability. The use of a metal oxide precursor nanostructure allows
49 significant control of the catalyst morphology and the ability to use various highly stable, non-
50 noble transition metal oxides beyond nickel oxide which may provide a pathway to increasing
51
52
53
54
55
56
57

1
2
3 stability. The ability to create metallic nanoarchitectures with controlled surface structures within
4
5 a carbon-free interconnected network that provides 3D molecular accessibility allows the design
6
7 of self-supported catalysts with high activity and extended durability for proton exchange
8
9 membrane fuel cells and other applications.
10
11
12
13
14

15 **4. Methods**

16
17 **Chemicals.** Iridium chloride hydrate ($\text{IrCl}_3 \cdot x\text{H}_2\text{O}$, 99.8%), nickel nitrate hexahydrate
18
19 ($\text{Ni}(\text{NO}_3)_2 \cdot 6\text{H}_2\text{O}$, 98%) and urea (N_2COH_4 , 99.3%) were obtained from Alfa Aesar. Ethylene
20
21 glycol, isopropanol (HPLC grade), and ACS grade water ($\geq 18 \text{ M}\Omega\text{-cm}$) were obtained from VWR
22
23 Analytical. All reagents were used without further purification.
24
25

26
27 **Synthesis of $\alpha\text{-Ni}(\text{OH})_2$ and NiO Nanosheets.** The $\alpha\text{-Ni}(\text{OH})_2$ nanosheets were
28
29 synthesized using a microwave-assisted hydrothermal process adapted from previously reported
30
31 methods.^{19,75} To prepare the $\alpha\text{-Ni}(\text{OH})_2$ nanosheets, 6.0 g (20.6 mmol) of $\text{Ni}(\text{NO}_3)_2 \cdot 6\text{H}_2\text{O}$ was
32
33 combined with 4.92 g (82 mmol) of urea, 18 mL of ultrapure water ($\geq 18 \text{ M}\Omega\text{-cm}$) and 126 mL of
34
35 ethylene glycol (EG). The solution was then divided into six aliquots (24 mL each) which were
36
37 placed in a Discover SP Microwave Reactor and then treated under variable microwave radiation
38
39 power using a controlled temperature of 120 °C which was maintained for 13 minutes under active
40
41 stirring. The obtained light green powder was recovered by centrifugation (1690 RCF, 3 min,
42
43 Thermo, Sorvall ST16) and subsequently rinsed five times with water and two times with
44
45 isopropanol using the same centrifuge conditions. Following the rinsing steps, the powder was
46
47 dried under vacuum at 60 °C overnight. To prepare NiO nanosheets, 0.18 g of $\text{Ni}(\text{OH})_2$ nanosheets
48
49 were heated within a muffle furnace (Thermolyne, Thermo Scientific, Inc.) from room temperature
50
51
52
53
54
55
56
57
58
59
60

1
2
3 to 300 °C for 90 minutes in ambient air using a ramp rate of 20 °C/min. After the 90 minute dwell
4
5 time, the sample was allowed to cool to room temperature, and then taken out from furnace.
6
7

8 **Synthesis of iridium-decorated NiO Nanosheets (NiO:Ir).** The NiO nanosheets were
9
10 decorated with Ir by modification of a previously reported synthesis method.⁷⁶ To deposit Ir on
11
12 the NiO nanosheets, 0.5 g of the prepared NiO was dispersed in 50 mL of ultrapure water using an
13
14 ultrasonic bath. In a second beaker, an appropriate amount of IrCl₃·xH₂O (52.46-53.29 wt. % Ir;
15
16 different batches had slightly different wt% Ir based on from information provided by the
17
18 manufacturer), corresponding to 21.0 wt % of metallic Ir vs NiO, was dissolved in 50 mL of
19
20 ultrapure water and then added to the NiO slurry. The specific amount of IrCl₃·xH₂O utilized was
21
22 based on the information obtained from the manufacturer for the % Ir within the specific batch (for
23
24 the IrCl₃·xH₂O with 53.29 wt. % Ir, 0.197 g was utilized to obtain 21.0 wt % of metallic Ir vs
25
26 NiO). Additional water was then added to obtain a total volume of 125 mL. The suspension was
27
28 separated into five 25 mL aliquots which were transferred to the microwave reactor and then
29
30 treated under variable microwave radiation power using a controlled temperature of 120 °C
31
32 maintained for 13 minutes under active stirring. This process was repeated for each aliquot.
33
34 Finally, a gray powder was recovered, rinsed, and dried as described above. The Ir-decorated NiO
35
36 nanosheets were notated as NiO:Ir. Analysis of the elemental composition of NiO:Ir using EDS
37
38 analysis showed 9.5 ± 1.8 wt % Ir within the material (ESI, Figure S2) which indicated that ~45
39
40 % of Ir from the IrCl₃·xH₂O precursor (21 wt % Ir relative to NiO used within the synthesis
41
42 process) was deposited onto the NiO nanosheets.
43
44
45
46
47
48

49 **Synthesis of 2D Ni-Ir nanoframes.** The NiO:Ir catalyst was thermally treated at either
50
51 200 °C or 300 °C for 23 min under 120 mL min⁻¹ flowing H₂/Ar (5/95 vol %) using a ramp rate of
52
53 20 °C min⁻¹ starting from room temperature. After a dwell time of 23 minutes, the reactor was
54
55
56
57

1
2
3 removed from the oven and allowed to cool under Ar/H₂ flow until reaching room temperature.
4
5 The synthesized samples were notated as NiIr-200 and NiIr-300 for the samples heated to either
6
7 200 °C or 300 °C respectively.
8
9

10 **Chemical leaching.** In order to chemically leach out unstable nickel from the material, 0.2
11 g of the as-prepared NiIr nanoframes was dispersed in 100 mL of 0.05 M HNO₃. The solution was
12 bubbled with Ar for 20 min then heated to 80 °C for 2 hours under magnetic stirring and under
13
14
15
16
17
18
19
20
21
22
23
24
25
26
27
28
29
30
31
32
33
34
35
36
37
38
39
40
41
42
43
44
45
46
47
48
49
50
51
52
53
54
55
56
57
58
59
60

chemically leached material was then recovered, rinsed, and dried as described above. The solutions used for the chemical leaching step for NiIr-200 and NiIr-300 were analyzed using Atomic Absorption (AA) spectroscopy to determine the amounts of Ni and Ir dissolved into the solution during the acid treatment. The AA measurements were obtained with a Perkin Elmer (Model PinAAcle900F) AA spectrometer using a nitrous oxide-acetylene flame and lamps to measure absorbance at 341.5 nm (Ni) and 263.97 nm (Ir). Standard solutions of Ni(NO₃)₂·6H₂O and IrCl₃·xH₂O were used for calibrating the absorbances of Ni and Ir with concentration. The chemically leached materials were notated as NiIr-200-CL, and NiIr-300-CL respectively. The wt % Ir and wt % Ni of NiIr-200-CL was determined by inductively coupled plasma atomic emission spectroscopy (ICP-AES) carried out by Galbraith Laboratories, Inc. (Knoxville, TN). From ICP analysis, the NiIr-200-CL catalyst was determined to be 65.5 wt % Ir and 18.0 % Ni. For the NiIr-300-CL catalyst, the Ir and Ni content was determined from ICP analysis to be 63.0 wt % Ir and 18.7 % Ni.

59
60

Physical and Structural Characterization. Powder X-ray diffraction (XRD) measurements were conducted using a Bruker AXS D8 Advance powder X-ray diffractometer with a Cu K α ($\lambda = 1.5406 \text{ \AA}$) radiation source, operating at 40 kV and 25 mA and a high resolution

1
2
3 energy dispersive 1D Linxeye XE detector. The scan range of 2θ was $5^\circ < 2\theta < 85^\circ$ with a 0.01°
4
5 increment. Nitrogen physisorption measurements were obtained using a Micromeritics ASAP
6
7 2020 surface area and porosimetry analyzer. Before analysis, the samples were degassed under
8
9 vacuum at 120°C for 16 h. Brunauer–Emmett–Teller (BET) surface areas were obtained from the
10
11 nitrogen physisorption isotherms. Mean pore diameters and cumulative pore volumes were
12
13 calculated from the adsorption isotherm using the Barrett-Joyner-Halenda (BJH) method
14
15 (Micromeritics Microactive software, version 4.02). Shown in Figure S5 is a representative
16
17 isotherm and pore distribution plot (incremental pore volume vs pore size) of NiIr-200-CL.
18
19
20
21

22 The morphology and elemental distribution of the catalysts were determined by scanning
23
24 electron microscopy (SEM) using a SEM FEI-Helios Nanolab 400. Cs-corrected scanning
25
26 transmission electron microscopy (STEM) was carried out by using a JEM-ARM200F (200 kV,
27
28 JEOL) equipped with an energy dispersed spectrometer (EDAX Silicon Drift detector). High angle
29
30 annular dark field STEM (HAADF-STEM) was obtained with a convergence angle of 26 mrad
31
32 and a collection semiangles from 50 to 180 mrad. The probe size used was about 0.09 nm with the
33
34 probe current of 22 pA. X-ray photoelectron spectra were obtained using a Thermo Scientific K
35
36 Alpha+ instrument using an Al $K\alpha$ X-ray source and an accelerating voltage of 200 keV. Survey
37
38 spectra were obtained using a pass energy of 200 eV, 20 scans, and a step size of 1 eV, and high-
39
40 resolution spectra were obtained at pass energy of 20 eV by averaging 20-50 scans collected with
41
42 a step size of 0.1 eV. The energies of the photoelectron peaks were referenced to the C 1s binding
43
44 energy of 284.8 eV for adventitious carbon. Peak fitting was performed by using a least squares
45
46 algorithm within Avantage software (Thermo Scientific, version 5.982) with a mixed Shirley-
47
48 Tougaard baseline and a Gaussian–Lorentzian product function for each peak. For fitting the Ni $2p$
49
50 region of the XPS spectrum, a spectral window that included both the Ni $2p_{3/2}$ and Ni $2p_{1/2}$ regions
51
52
53
54
55
56
57

1
2
3 was used for determining the baseline. Based on the large spin-orbit splitting of the Ni $2p_{3/2}$ and
4 Ni $2p_{1/2}$ peaks, fitting was performed only on the Ni $2p_{3/2}$ region as supported by a prior study.³⁸
5
6

7
8 **Rotating Disk Electrochemical Characterization.** The electrochemical measurements
9
10 were conducted at constant temperature (298 K) in a three-electrode cell using a thin-film rotating
11 disk electrode (RDE) configuration. Electrodes were prepared and RDE measurements were
12 obtained at both Texas State University and the National Renewable Energy Laboratory (NREL).
13 RDE measurements obtained Texas State University utilized an Autolab PGSTAT128N
14 bipotentiostat and rotation control (Pine Instruments). For RDE measurements performed at Texas
15 State University, a gold disk electrode (RDE, Pine Research instrument, geometric area: 0.196
16 cm^2) with a thin film of the prepared catalyst was used as the working electrode, and a Pt mesh
17 and a freshly prepared reversible hydrogen electrode (RHE) were used as counter and reference
18 electrodes, respectively. The electrode fabrication and RDE testing protocols were based on
19 methods previously reported.⁶ Catalyst inks were prepared by combining a specific mass
20 (typically ~ 3 mg) of the acid-leached catalysts (NiIr-200-CL or NiIr-300-CL) with a specific
21 volume of a stock solution to yield a catalyst concentration of $0.7 \text{ mg}_{\text{cat}} \text{ mL}^{-1}$. The stock solution
22 was prepared by mixing 0.4 mL of Nafion suspension (Aldrich, 5 wt %, 1100 g equivalent weight),
23 20 mL of isopropanol, and 79.6 mL ultra-pure water ($\geq 18 \text{ M}\Omega\text{-cm}$). The inks were sonicated
24 (Fisher, 40 kHz) in an ice-bath for 20 minutes, and then treated with a probe sonicator for 20
25 seconds while surrounded by an ice bath. The ink was then immersed in a controlled temperature
26 bath (25 °C) for 1 minute while maintaining agitation and then used immediately. For comparison
27 with the synthesized catalysts, inks were also prepared with commercially available IrO_2 (Alfa
28 Aesar, Product number 43396). For the IrO_2 the catalyst ink consisted of $0.53 \text{ mg}_{\text{cat}} \text{ mL}^{-1}$ (84 wt
29 % Ir). The inks were applied to a polished Au working electrode (0.196 cm^2 geometric area) while
30
31
32
33
34
35
36
37
38
39
40
41
42
43
44
45
46
47
48
49
50
51
52
53
54
55
56
57

1
2
3 under rotation (200 rpm) based on the previously reported approach of rotational drying.⁷⁷ The
4
5 electrode loading was controlled by depositing a specific volume of the ink onto the Au working
6
7 electrode. For the NiIr-200-CL or NiIr-300-CL catalysts, 5 μL was deposited onto the Au electrode
8
9 which corresponds to a loading of $11.7 \mu\text{g}_{\text{Ir}} \text{cm}_{\text{geo}}^{-2}$ for NiIr-200-CL (65.5 wt % Ir) and $9.1 \mu\text{g}_{\text{Ir}}$
10
11 $\text{cm}_{\text{geo}}^{-2}$ for NiIr-300-CL (63.0 wt % Ir). After depositing the inks on the rotating Au electrode, the
12
13 inks were maintained under rotation and allowed to dry under ambient conditions. For electrode
14
15 preparation and RDE measurements obtained at NREL, identical procedures and protocols as
16
17 described above were utilized with the exception of the following: a Autolab PGSTAT302N
18
19 potentiostat/galvanostat was used; a Au mesh (rather than a Pt mesh) was used as the counter
20
21 electrode; the ink was applied using a rotation rate of 100 rpm to coat the ink onto the electrode;
22
23 and 700 rpm was used for drying the electrode. Similar OER mass activities within experimental
24
25 error were obtained for the catalysts tested at Texas State University and NREL.
26
27
28
29
30

31 The electrochemical characterization of the catalysts was carried out in 0.1 M HClO_4
32
33 electrolyte prepared with 70% HClO_4 (Veritas Doubly Distilled, GFS Chemicals) ($0.000001\% \text{Cl}^-$)
34
35 and ACS grade water ($\geq 18 \text{ M}\Omega\text{-cm}$) based on methods previously reported.⁶ For the
36
37 electrochemical tests, the Au working electrode was placed in a three-electrode cell with the 0.1
38
39 M HClO_4 electrolyte. A Pt mesh and a freshly prepared reversible hydrogen electrode (RHE) were
40
41 used as counter and reference electrodes, respectively. The electrodes were immersed in Argon
42
43 saturated 0.1 M HClO_4 under potential control ($0.1 V_{\text{RHE}}$). The catalysts were first conditioned by
44
45 cycling 20 times from $0.05\text{-}1.0 V_{\text{RHE}}$ at 100 mV s^{-1} and 2500 rpm. The electrochemical surface
46
47 area of metallic Ir (ECSA_{Ir}) was calculated by CO-stripping using a specific charge of $358 \mu\text{C}$
48
49 $\text{cm}_{\text{Ir}}^{-2}$ as the charge corresponding to desorption of an adsorbed monolayer of CO.²⁵ Prior to the
50
51 analysis in OER potential range, the catalysts were electrochemically conditioned by cycling
52
53
54
55
56
57
58
59
60

1
2
3 between 0.05 to 1.5 V_{RHE} for 60 cycles at a scan rate of 100 mV s^{-1} in Argon-saturated 0.1 M
4 HClO_4 . After the electrochemical conditioning step to 1.5 V_{RHE} , the electrochemical surface area
5 of IrO_2 ($\text{ECSA}_{\text{IrO}_2}$) was determined by measuring the pseudocapacitive charge between 0.3 V and
6 1.25 V obtained using a scan rate of 50 mV s^{-1} and by subtracting the contribution of the Au disk
7 current collector. The electrochemical surface area was calculated based on the background-
8 subtracted pseudocapacitive charge and the coulombic conversion factor of $596 \mu\text{C cm}_{\text{IrO}_2}^{-2}$.²⁴
9

10
11 For evaluating the oxygen evolution reaction activity, the electrode was then conditioned
12 by cycling 10 times in the potential range 1.2-1.8 V_{RHE} at 100 mV s^{-1} and under 2500 rpm rotation.
13 Linear sweep voltammetry (LSV) in the potential range of 1.2-1.8 V_{RHE} was performed using a
14 scan rate of 20 mV s^{-1} and a rotation rate of 2500 rpm. Steady-state (iR-corrected)
15 chronoamperometric measurements were then performed by gradually stepping the potential at steps
16 of 0.01 V from 1.3 to 1.6 V_{RHE} while holding for 5 seconds at each potential and rotating the
17 working electrode at 2500 rpm. The internal resistance (iR) values (23-27 Ω) were determined
18 prior to every evaluation using the current interruption method at 1.6 V_{RHE} . The data obtained from
19 chronoamperometric measurements was used for the Tafel plots and for determining the OER mass
20 activity and specific activity. The mass-normalized OER activity was determined by the current
21 at a specific voltage from the chronoamperometric measurements divided by the Ir mass on the
22 electrode. Inspection of the Tafel plots for linear behavior within specific voltage ranges was used
23 to evaluate that the electrode was not within a mass-transport limited regime within the specific
24 voltage range. Tafel slopes were determined using current obtained from chronoamperometry
25 measurements using the iR-corrected potential between 1.47 V_{RHE} to 1.52 V_{RHE} . After the
26 evaluation of the electrocatalyst in the OER potential range, CV measurements were again
27
28
29
30
31
32
33
34
35
36
37
38
39
40
41
42
43
44
45
46
47
48
49
50
51
52
53
54
55
56
57
58
59
60

1
2
3 obtained to determine the nature of the surface condition after exposure to OER potentials of up
4
5 to 1.8 V_{RHE}.
6

7
8 Following the measurements of the OER activity, an accelerated durability test was carried
9
10 out by maintaining the electrode at a constant potential of 1.6 V_{RHE} for 13.5 hours under a rotation
11
12 rate of 2500 rpm. After the constant potential step was completed, the electrolyte was replaced,
13
14 and cyclic voltammetry (CV), LSV, and chronoamperometry measurements were obtained as
15
16 described above. During LSV and chronoamperometry tests, to account for solution resistance the
17
18 internal resistance was corrected by the potentiostat using a resistance of 25 Ω. After the stability
19
20 tests, CO stripping tests were also performed.
21
22

23
24 **Computational details.** All calculations were performed using the Vienna *ab Initio*
25
26 Simulation Package (VASP)⁷⁸⁻⁸⁰ with spin polarization and the revised Perdew-Burke-Ernzerhof
27
28 generalized gradient approximation (GGA-RPBE) functional. The RPBE functional has been
29
30 shown to improve the adsorption energies of atoms and molecules on transition-metal surfaces.⁸¹
31
32 Electron-ion interactions were described by the projector augmented wave (PAW)
33
34 pseudopotentials.⁸²⁻⁸³ The tetrahedron method with Blöchl corrections was used to represent partial
35
36 occupancies. The cut off energy for the plane-wave basis expansion was chosen to be 400 eV. The
37
38 convergence criteria for electronic self-consistent iteration and ionic relaxation were set to 10⁻⁴
39
40 and 10⁻³ eV, respectively. In order to model the NiIrO_x system, a Ni-doped IrO₂ surface was
41
42 considered. The pristine IrO₂ surface was modeled as described in our previous study⁸: first, the
43
44 pristine IrO₂ bulk structure was fully optimized. After bulk relaxation, a 4-layer (110) IrO₂ surface
45
46 was cleaved with a 2x1 supercell. For the slab calculations, the Brillouin zone was sampled using
47
48 an 11x11x1 Monkhorst-Pack k-point mesh and a 16 Å vacuum space was allowed in the z direction
49
50 to avoid artificial interactions. Here the two bottom layers were kept fixed while the top two layers
51
52
53
54
55
56
57
58
59
60

1
2
3 were allowed to relax. The resulting (110) surface is formed by four iridium atoms: two penta-
4 coordinated (5-Ir) and two hexa-coordinated (6-Ir). The surface also contains two types of oxygen
5 atoms: bridge (O_b) and three-coordinated (O_t) oxygen atoms, which are located above and on the
6 plane of the metal atoms, respectively, see Figure 7a for details. Finally, in order to represent the
7 different regions of the electrocatalyst, two doped- IrO_2 models were obtained depending on the
8 doping site; Ni substitutes either one penta-coordinated (5-Ni) or one hexa-coordinated (6-Ni) Ir
9 atom on the surface. It is worth mentioning that the addition of Ni at the surface level forms
10 different adsorption sites and provides more direct insights on the effect of the Ni on the OER, as
11 discussed in the text.
12
13
14
15
16
17
18
19
20
21
22

23
24 The adsorption energy (ΔE_{ads}) of an adsorbate j was calculated using the following
25 equation: $\Delta E_{\text{ads}} = E_{\text{sys}} - (E_j - E_{\text{surf}})$, where E_{sys} , E_{surf} , and E_j are the energies of the
26 adsorbate/slab complex, surface slab, and adsorbate. The energy of the adsorbates was computed
27 by optimizing the geometry of the species in a simulation box with large vacuum to avoid self-
28 interactions. Although some functionals are considered to be non-suited for molecular oxygen
29 energy calculations, the reported trends are still within good agreement with the experimental
30 observations. Activation energies were calculated using the climbing nudged elastic band (cNEB)
31 method.⁸⁴⁻⁸⁵ This method optimizes a number of intermediate images along a reaction path, where
32 the initial image is the reactant and the final is the product. In this case, at least 5 intermediate
33 images were used. In addition, the charge transfer was studied by using the Bader charge analysis⁸⁶⁻
34
35
36
37
38
39
40
41
42
43
44
45
46
47
48
49
50
51
52
53
54
55
56
57
58
59
60

88 in which the total electronic charge of an atom is approximated by the charge enclosed in the
volume defined by zero flux surfaces.

ACKNOWLEDGEMENT

1
2
3 C.P.R. acknowledges support from the Office of Naval Research (Grant No. N00014-16-
4 1-2777) and the National Science Foundation PREM (Grant No. DMR-1205670). P.B.B and
5
6 L.E.C.F gratefully acknowledge supercomputer resources from the Texas A&M University High
7
8 Performance Computer Center and Texas Advanced Computing Center (TACC). R.M.C and
9
10 M.J.A-J. acknowledge the Kleberg Advanced Microscopy Center. The work was supported by
11
12 the U.S. Department of Energy with Alliance for Sustainable Energy, LLC, the Manager and
13
14 Operator of the National Renewable Energy Laboratory. Funding provided by the U.S. Department
15
16 of Energy Office of Energy Efficiency and Renewable Energy Fuel Cell Technologies Office. The
17
18 views and opinions of the authors expressed herein do not necessarily state or reflect those of the
19
20 United States Government or any agency thereof. Neither the United States Government nor any
21
22 agency thereof, nor any of their employees, makes any warranty, expressed or implied, or assumes
23
24 any legal liability or responsibility for the accuracy, completeness, or usefulness of any
25
26 information, apparatus, product, or process disclosed, or represents that its use would not infringe
27
28 privately owned rights. The U.S. Government retains and the publisher, by accepting the article
29
30 for publication, acknowledges that the U.S. Government retains a nonexclusive, paid-up,
31
32 irrevocable, worldwide license to publish or reproduce the published form of this work, or allow
33
34 others to do so, for U.S. Government purposes.
35
36
37
38
39
40
41
42
43
44

45 **ASSOCIATED CONTENT**

46
47
48 **Supporting Information:** SEM, XRD, STEM images and elemental mapping of precursor
49
50 materials and NiIr-200-CL and NiIr-300-CL electrocatalysts; electrochemical data (CVs, CO
51
52 stripping, OER activities); nitrogen physisorption isotherms; XPS fitting analysis.
53
54
55
56
57

AUTHOR INFORMATION

Corresponding author

*Email: cprhodes@txstate.edu; Phone: 512-245-6721. Fax: 512-245-2374

ORCID

Christopher P. Rhodes: 0000-0003-4886-9875

Shaun M. Alia: 0000-0002-7647-9383

Notes

The authors declare no competing financial interests.

References

(1) Spori, C.; Kwan, J. T. H.; Bonakdarpour, A.; Wilkinson, D. P.; Strasser, P., The Stability Challenges of Oxygen Evolving Catalysts: Towards a Common Fundamental Understanding and Mitigation of Catalyst Degradation. *Angew. Chem.-Int. Edit.* **2017**, *56*, 5994-6021.

(2) Fabbri, E.; Haberer, A.; Waltar, K.; Kotz, R.; Schmidt, T. J., Developments and Perspectives of Oxide-Based Catalysts for the Oxygen Evolution Reaction. *Catal. Sci. Technol.* **2014**, *4*, 3800-3821.

(3) Reier, T.; Nong, H. N.; Teschner, D.; Schlogl, R.; Strasser, P., Electrocatalytic Oxygen Evolution Reaction in Acidic Environments - Reaction Mechanisms and Catalysts. *Adv. Energy Mater.* **2017**, *7*, 1601275.

(4) Suen, N. T.; Hung, S. F.; Quan, Q.; Zhang, N.; Xu, Y. J.; Chen, H. M., Electrocatalysis for the Oxygen Evolution Reaction: Recent Development and Future Perspectives. *Chem. Soc. Rev.* **2017**, *46*, 337-365.

(5) Alia, S. M.; Shulda, S.; Ngo, C.; Pylypenko, S.; Pivovar, B. S., Iridium-Based Nanowires as Highly Active, Oxygen Evolution Reaction Electrocatalysts. *ACS Catal.* **2018**, *8*, 2111-2120.

(6) Alia, S. M.; Rasimick, B.; Ngo, C.; Neyerlin, K. C.; Kocha, S. S.; Pylypenko, S.; Xu, H.; Pivovar, B. S., Activity and Durability of Iridium Nanoparticles in the Oxygen Evolution Reaction. *J. Electrochem. Soc.* **2016**, *163*, F3105-F3112.

(7) Petrykin, V.; Bastl, Z.; Franc, J.; Macounova, K.; Makarova, M.; Mukerjee, S.; Ramaswamy, N.; Spirovova, I.; Krtil, P., Local Structure of Nanocrystalline Ru_{1-x}Ni_xO_{2-δ} Dioxide and Its Implications for Electrocatalytic Behavior-an XPS and XAS Study. *J. Phys. Chem. C* **2009**, *113*, 21657-21666.

(8) Gonzalez-Huerta, R. G.; Ramos-Sanchez, G.; Balbuena, P. B., Oxygen Evolution in Co-Doped RuO₂ and IrO₂: Experimental and Theoretical Insights to Diminish Electrolysis Overpotential. *J. Power Sources* **2014**, *268*, 69-76.

(9) Reier, T.; Pawolek, Z.; Cherevko, S.; Bruns, M.; Jones, T.; Teschner, D.; Selve, S.; Bergmann, A.; Nong, H. N.; Schlogl, R.; Mayrhofer, K. J. J.; Strasser, P., Molecular Insight in

1
2
3 Structure and Activity of Highly Efficient, Low-Ir Ir-Ni Oxide Catalysts for Electrochemical
4 Water Splitting (OER). *J. Am. Chem. Soc.* **2015**, *137*, 13031-13040.

5 (10) Halck, N. B.; Petrykin, V.; Krtil, P.; Rossmeisl, J., Beyond the Volcano Limitations
6 in Electrocatalysis - Oxygen Evolution Reaction. *Phys. Chem. Chem. Phys.* **2014**, *16*, 13682-
7 13688.

8 (11) Nong, H. N.; Oh, H. S.; Reier, T.; Willinger, E.; Willinger, M. G.; Petkov, V.;
9 Teschner, D.; Strasser, P., Oxide-Supported IrNi_x Core-Shell Particles as Efficient, Cost-
10 Effective, and Stable Catalysts for Electrochemical Water Splitting. *Angew. Chem.-Int. Edit.* **2015**,
11 *54*, 2975-2979.

12 (12) Moghaddam, R. B.; Wang, C.; Sorge, J. B.; Brett, M. J.; Bergens, S. H., Easily
13 Prepared, High Activity Ir-Ni Oxide Catalysts for Water Oxidation. *Electrochem. Commun.* **2015**,
14 *60*, 109-112.

15 (13) Lim, J.; Yang, S.; Kim, C.; Roh, C. W.; Kwon, Y.; Kim, Y. T.; Lee, H., Shaped Ir-Ni
16 Bimetallic Nanoparticles for Minimizing Ir Utilization in Oxygen Evolution Reaction. *Chem.*
17 *Commun.* **2016**, *52*, 5641-5644.

18 (14) Xu, S.; Liu, Y.; Tong, J. L.; Hu, W.; Xia, Q. H., Iridium-Nickel Composite Oxide
19 Catalysts for Oxygen Evolution Reaction in Acidic Water Electrolysis. *Russ. J. Electrochem.* **2016**,
20 *52*, 1021-1031.

21 (15) Xu, S.; Chen, S. L.; Tian, L. H.; Xia, Q. H.; Hu, W., Selective-Leaching Method to
22 Fabricate an Ir Surface-Enriched Ir-Ni Oxide Electrocatalyst for Water Oxidation. *J. Solid State*
23 *Electrochem.* **2016**, *20*, 1961-1970.

24 (16) Geiger, S.; Kasian, O.; Mingers, A. M.; Nicley, S. S.; Haenen, K.; Mayrhofer, K. J. J.;
25 Cherevko, S., Catalyst Stability Benchmarking for the Oxygen Evolution Reaction: The
26 Importance of Backing Electrode Material and Dissolution in Accelerated Aging Studies.
27 *ChemSusChem* **2017**, *10*, 4140-4143.

28 (17) Seitz, L. C.; Dickens, C. F.; Nishio, K.; Hikita, Y.; Montoya, J.; Doyle, A.; Kirk, C.;
29 Vojvodic, A.; Hwang, H. Y.; Norskov, J. K.; Jaramillo, T. F., A Highly Active and Stable
30 Iro_x/Siro₃ Catalyst for the Oxygen Evolution Reaction. *Science* **2016**, *353*, 1011-1014.

31 (18) Luc, W.; Jiao, F., Nanoporous Metals as Electrocatalysts: State-of-the-Art,
32 Opportunities, and Challenges. *ACS Catal.* **2017**, *7*, 5856-5861.

33 (19) Godinez-Salomon, F.; Mendoza-Cruz, R.; Arellano-Jimenez, M. J.; Jose-Yacaman,
34 M.; Rhodes, C. P., Metallic Two-Dimensional Nanoframes: Unsupported Hierarchical Nickel-
35 Platinum Alloy Nanoarchitectures with Enhanced Electrochemical Oxygen Reduction Activity
36 and Stability. *ACS Appl. Mater. Interfaces* **2017**, *9*, 18660-18674.

37 (20) Cherevko, S.; Kulyk, N.; Mayrhofer, K. J. J., Durability of Platinum-Based Fuel Cell
38 Electrocatalysts: Dissolution of Bulk and Nanoscale Platinum. *Nano Energy* **2016**, *29*, 275-298.

39 (21) Liu, W.; Rodriguez, P.; Borchardt, L.; Foelske, A.; Yuan, J. P.; Herrmann, A. K.;
40 Geiger, D.; Zheng, Z. K.; Kaskel, S.; Gaponik, N.; Kotz, R.; Schmidt, T. J.; Eychmuller, A.,
41 Bimetallic Aerogels: High-Performance Electrocatalysts for the Oxygen Reduction Reaction.
42 *Angew. Chem.-Int. Edit.* **2013**, *52*, 9849-9852.

43 (22) Rolison, D. R., Catalytic Nanoarchitectures - the Importance of Nothing and the
44 Unimportance of Periodicity. *Science* **2003**, *299*, 1698-1701.

45 (23) Koresh, J.; Soffer, A., Double Layer Capacitance and Charging Rate of
46 Ultramicroporous Carbon Electrodes. *J. Electrochem. Soc.* **1977**, *124*, 1379-1385.

(24) Zhao, S.; Yu, H. R.; Maric, R.; Danilovic, N.; Capuano, C. B.; Ayers, K. E.; Mustain, W. E., Calculating the Electrochemically Active Surface Area of Iridium Oxide in Operating Proton Exchange Membrane Electrolyzers. *J. Electrochem. Soc.* **2015**, *162*, F1292-F1298.

(25) Alia, S. M.; Hurst, K. E.; Kocha, S. S.; Pivovar, B. S., Mercury Underpotential Deposition to Determine Iridium and Iridium Oxide Electrochemical Surface Areas. *J. Electrochem. Soc.* **2016**, *163*, F3051-F3056.

(26) Beverskog, B.; Puigdomenech, I., Revised Pourbaix Diagrams for Nickel at 25-300 Degrees C. *Corrosion Sci.* **1997**, *39*, 969-980.

(27) Kikuchi, N.; Seo, M., In Situ Gravimetry of Nickel Thin Film During Potentiodynamic Polarization in Acidic and Alkaline Sulfate Solutions. *Corrosion Sci.* **2006**, *48*, 994-1003.

(28) Nakamura, M.; Ikemiya, N.; Iwasaki, A.; Suzuki, Y.; Ito, M., Surface Structures at the Initial Stages in Passive Film Formation on Ni(111) Electrodes in Acidic Electrolytes. *J. Electroanal. Chem.* **2004**, *566*, 385-391.

(29) Sasaki, K.; Kuttiyiel, K. A.; Barrio, L.; Su, D.; Frenkel, A. I.; Marinkovic, N.; Mahajan, D.; Adzic, R. R., Carbon-Supported IrNi Core-Shell Nanoparticles: Synthesis, Characterization, and Catalytic Activity. *J. Phys. Chem. C* **2011**, *115*, 9894-9902.

(30) Zhao, Y. S.; Zhang, J. Z., Microstrain and Grain-Size Analysis from Diffraction Peak Width and Graphical Derivation of High-Pressure Thermomechanics. *J. Appl. Crystallogr.* **2008**, *41*, 1095-1108.

(31) Chattot, R.; Le Bacq, O.; Beermann, V.; Kuhl, S.; Herranz, J.; Henning, S.; Kuhn, L.; Asset, T.; Guetaz, L.; Renou, G.; Drnec, J.; Bordet, P.; Pasturel, A.; Eychmuller, A.; Schmidt, T. J.; Strasser, P.; Dubau, L.; Maillard, F., Surface Distortion as a Unifying Concept and Descriptor in Oxygen Reduction Reaction Electrocatalysis. *Nature Materials* **2018**, *17*, 827-833.

(32) Ahmadi, M.; Behafarid, F.; Cui, C. H.; Strasser, P.; Cuenya, B. R., Long-Range Segregation Phenomena in Shape-Selected Bimetallic Nanoparticles: Chemical State Effects. *ACS Nano* **2013**, *7*, 9195-9204.

(33) Zhao, Z.; Wang, F. H.; Fisher, A.; Shen, Y. C.; Cheng, D. J., Phase Stability and Segregation Behavior of Nickel-Based Nanoalloys Based on Theory and Simulation. *J. Alloy. Compd.* **2017**, *708*, 1150-1160.

(34) Guisbiers, G.; Mendoza-Perez, R.; Bazan-Diaz, L.; Mendoza-Cruz, R.; Velazquez-Salazar, J. J.; Jose-Yacamán, M., Size and Shape Effects on the Phase Diagrams of Nickel-Based Bimetallic Nanoalloys. *J. Phys. Chem. C* **2017**, *121*, 6930-6939.

(35) Biesinger, M. C.; Payne, B. P.; Lau, L. W. M.; Gerson, A.; Smart, R. S. C., X-Ray Photoelectron Spectroscopic Chemical State Quantification of Mixed Nickel Metal, Oxide and Hydroxide Systems. *Surf. Interface Anal.* **2009**, *41*, 324-332.

(36) Freakley, S. J.; Ruiz-Esquius, J.; Morgan, D. J., The X-Ray Photoelectron Spectra of Ir, IrO₂ and IrCl₃ Revisited. *Surf. Interface Anal.* **2017**, *49*, 794-799.

(37) McIntyre, N. S.; Cook, M. G., X-Ray Photoelectron Studies on Some Oxides and Hydroxides of Cobalt, Nickel, and Copper. *Anal. Chem.* **1975**, *47*, 2208-2213.

(38) Biesinger, M. C.; Payne, B. P.; Grosvenor, A. P.; Lau, L. W. M.; Gerson, A. R.; Smart, R. S., Resolving Surface Chemical States in XPS Analysis of First Row Transition Metals, Oxides and Hydroxides: Cr, Mn, Fe, Co and Ni. *Appl. Surf. Sci.* **2011**, *257*, 2717-2730.

(39) Abbott, D. F.; Lebedev, D.; Waltar, K.; Povia, M.; Nachtegaal, M.; Fabbri, E.; Coperet, C.; Schmidt, T. J., Iridium Oxide for the Oxygen Evolution Reaction: Correlation between Particle Size, Morphology, and the Surface Hydroxo Layer from Operando XAS. *Chem. Mat.* **2016**, *28*, 6591-6604.

(40) Cherevko, S.; Geiger, S.; Kasian, O.; Mingers, A.; Mayrhofer, K. J. J., Oxygen Evolution Activity and Stability of Iridium in Acidic Media. Part 1. - Metallic Iridium. *J. Electroanal. Chem.* **2016**, *773*, 69-78.

(41) Cruz, M. S.; Tejera, M. J. G.; Villamanan, M. C., Electrochemical Reduction of the Clo_4^- Ion on the Iridium Electrode. *Electrochim. Acta* **1985**, *30*, 1563-1569.

(42) Pajkossy, T.; Kibler, L. A.; Kolb, D. M., Voltammetry and Impedance Measurements of Ir(100) Electrodes in Aqueous Solutions. *J. Electroanal. Chem.* **2007**, *600*, 113-118.

(43) Godinez-Salomon, F.; Rhodes, C. P.; Alcantara, K. S.; Zhu, Q. S.; Canton, S. E.; Calderon, H. A.; Reyes-Rodriguez, J. L.; Leyva, M. A.; Solorza-Feria, O., Tuning the Oxygen Reduction Activity and Stability of $\text{Ni}(\text{OH})_2/\text{Pt}/\text{C}$ Catalysts through Controlling Pt Surface Composition, Strain, and Electronic Structure. *Electrochim. Acta* **2017**, *247*, 958-969.

(44) van der Vliet, D. F.; Wang, C.; Li, D. G.; Paulikas, A. P.; Greeley, J.; Rankin, R. B.; Strmcnik, D.; Tripkovic, D.; Markovic, N. M.; Stamenkovic, V. R., Unique Electrochemical Adsorption Properties of Pt-Skin Surfaces. *Angew. Chem.-Int. Edit.* **2012**, *51*, 3139-3142.

(45) Oh, H. S.; Nong, H. N.; Reier, T.; Gliech, M.; Strasser, P., Oxide-Supported Ir Nanodendrites with High Activity and Durability for the Oxygen Evolution Reaction in Acid PEM Water Electrolyzers. *Chem. Sci.* **2015**, *6*, 3321-3328.

(46) Steegstra, P.; Busch, M.; Panas, I.; Ahlberg, E., Revisiting the Redox Properties of Hydrous Iridium Oxide Films in the Context of Oxygen Evolution. *J. Phys. Chem. C* **2013**, *117*, 20975-20981.

(47) Cherevko, S.; Geiger, S.; Kasian, O.; Mingers, A.; Mayrhofer, K. J. J., Oxygen Evolution Activity and Stability of Iridium in Acidic Media. Part 2. - Electrochemically Grown Hydrous Iridium Oxide. *J. Electroanal. Chem.* **2016**, *774*, 102-110.

(48) Hillman, A. R.; Skopek, M. A.; Gurman, S. J., X-Ray Spectroscopy of Electrochemically Deposited Iridium Oxide Films: Detection of Multiple Sites through Structural Disorder. *Phys. Chem. Chem. Phys.* **2011**, *13*, 5252-5263.

(49) Grupioni, A. A. F.; Arashiro, E.; Lassali, T. A. F., Voltammetric Characterization of an Iridium Oxide-Based System: The Pseudocapacitive Nature of the $\text{Ir}_{0.3}\text{mn}_{0.7}\text{o}_2$ Electrode. *Electrochim. Acta* **2002**, *48*, 407-418.

(50) Lee, Y.; Suntivich, J.; May, K. J.; Perry, E. E.; Shao-Horn, Y., Synthesis and Activities of Rutile IrO_2 and RuO_2 Nanoparticles for Oxygen Evolution in Acid and Alkaline Solutions. *J. Phys. Chem. Lett.* **2012**, *3*, 399-404.

(51) Burke, L. D.; Whelan, D. P., A Voltammetric Investigation of the Charge Storage Reactions of Hydrous Iridium Oxide Layers. *J. Electroanal. Chem.* **1984**, *162*, 121-141.

(52) Li, Z.; Yu, R.; Huang, J. L.; Shi, Y. S.; Zhang, D. Y.; Zhong, X. Y.; Wang, D. S.; Wu, Y. E.; Li, Y. D., Platinum-Nickel Frame within Metal-Organic Framework Fabricated in Situ for Hydrogen Enrichment and Molecular Sieving. *Nat. Commun.* **2015**, *6*, 8.

(53) Lettenmeier, P.; Wang, L.; Golla-Schindler, U.; Gazdzicki, P.; Canas, N. A.; Handl, M.; Hiesgen, R.; Hosseiny, S. S.; Gago, A. S.; Friedrich, K. A., Nanosized $\text{Ir}_x\text{-Ir}$ Catalyst with Relevant Activity for Anodes of Proton Exchange Membrane Electrolysis Produced by a Cost-Effective Procedure. *Angew. Chem.-Int. Edit.* **2016**, *55*, 742-746.

(54) Moreno-Hernandez, I. A.; MacFarland, C. A.; Read, C. G.; Papadantonakis, K. M.; Brunshwig, B. S.; Lewis, N. S., Crystalline Nickel Manganese Antimonate as a Stable Water-Oxidation Catalyst in Aqueous 1.0 M H_2SO_4 . *Energy Environ. Sci.* **2017**, *10*, 2103-2108.

(55) Smith, R. D. L.; Sporinova, B.; Fagan, R. D.; Trudel, S.; Berlinguette, C. P., Facile Photochemical Preparation of Amorphous Iridium Oxide Films for Water Oxidation Catalysis. *Chem. Mat.* **2014**, *26*, 1654-1659.

(56) Mayrhofer, K. J. J.; Strmcnik, D.; Blizanac, B. B.; Stamenkovic, V.; Arenz, M.; Markovic, N. M., Measurement of Oxygen Reduction Activities Via the Rotating Disc Electrode Method: From Pt Model Surfaces to Carbon-Supported High Surface Area Catalysts. *Electrochim. Acta.* **2008**, *53*, 3181-3188.

(57) Arbabi, F.; Montazeri, H.; Abouatallah, R.; Wang, R.; Bazylak, A., Three-Dimensional Computational Fluid Dynamics Modelling of Oxygen Bubble Transport in Polymer Electrolyte Membrane Electrolyzer Porous Transport Layers. *J. Electrochem. Soc.* **2016**, *163*, F3062-F3069.

(58) Nouri-Khorasani, A.; Ojong, E. T.; Smolinka, T.; Wilkinson, D. P., Model of Oxygen Bubbles and Performance Impact in the Porous Transport Layer of Pem Water Electrolysis Cells. *Int. J. Hydrog. Energy* **2017**, *42*, 28665-28680.

(59) Li, Y. F.; Kang, Z. Y.; Mo, J. K.; Yang, G. Q.; Yu, S. L.; Talley, D. A.; Han, B.; Zhang, F. Y., In-Situ Investigation of Bubble Dynamics and Two-Phase Flow in Proton Exchange Membrane Electrolyzer Cells. *Int. J. Hydrog. Energy* **2018**, *43*, 11223-11233.

(60) Panchenko, O.; Borgardt, E.; Zwaygardt, W.; Hackemuller, F. J.; Bram, M.; Kardjilov, N.; Arlt, T.; Manke, I.; Muller, M.; Stolten, D.; Lehnert, W., In-Situ Two-Phase Flow Investigation of Different Porous Transport Layer for a Polymer Electrolyte Membrane (Pem) Electrolyzer with Neutron Spectroscopy. *J. Power Sources* **2018**, *390*, 108-115.

(61) Lebedev, D.; Povia, M.; Waltar, K.; Abdala, P. M.; Castelli, I. E.; Fabbri, E.; Blanco, M. V.; Fedorov, A.; Coperet, C.; Marzari, N.; Schmidt, T. J., Highly Active and Stable Iridium Pyrochlores for Oxygen Evolution Reaction. *Chem. Mat.* **2017**, *29*, 5182-5191.

(62) McCrory, C. C. L.; Jung, S.; Ferrer, I. M.; Chatman, S. M.; Peters, J. C.; Jaramillo, T. F., Benchmarking Hydrogen Evolving Reaction and Oxygen Evolving Reaction Electrocatalysts for Solar Water Splitting Devices. *J. Am. Chem. Soc.* **2015**, *137*, 4347-4357.

(63) Doyle, R. L.; Lyon, M. E. G., The Oxygen Evolution Reaction: Mechanistic Concepts and Catalyst Design. In *Photoelectrochemical Solar Fuel Production: From Basic Principles to Advanced Devices*, Giménez, S.; Bisquert, J., Eds. Springer International Publishing: Cham: **2016**, pp 41-104.

(64) Shinagawa, T.; Garcia-Esparza, A. T.; Takanabe, K., Insight on Tafel Slopes from a Microkinetic Analysis of Aqueous Electrocatalysis for Energy Conversion. *Sci. Rep.* **2015**, *5*, 13801.

(65) Fang, Y. H.; Liu, Z. P., Mechanism and Tafel Lines of Electro-Oxidation of Water to Oxygen on RuO₂(110). *J. Am. Chem. Soc.* **2010**, *132*, 18214-18222.

(66) Man, I. C.; Su, H. Y.; Calle-Vallejo, F.; Hansen, H. A.; Martinez, J. I.; Inoglu, N. G.; Kitchin, J.; Jaramillo, T. F.; Norskov, J. K.; Rossmeisl, J., Universality in Oxygen Evolution Electrocatalysis on Oxide Surfaces. *ChemCatChem* **2011**, *3*, 1159-1165.

(67) Bockris, J. O., Kinetics of Activation Controlled Consecutive Electrochemical Reactions: Anodic Evolution of Oxygen. *J. Chem. Phys.* **1956**, *24*, 817-827.

(68) Garcia-Mota, M.; Vojvodic, A.; Metiu, H.; Man, I. C.; Su, H. Y.; Rossmeisl, J.; Norskov, J. K., Tailoring the Activity for Oxygen Evolution Electrocatalysis on Rutile TiO₂(110) by Transition-Metal Substitution. *ChemCatChem* **2011**, *3*, 1607-1611.

(69) Rossmeisl, J.; Qu, Z. W.; Zhu, H.; Kroes, G. J.; Norskov, J. K., Electrolysis of Water on Oxide Surfaces. *J. Electroanal. Chem.* **2007**, *607*, 83-89.

(70) Feng, Q.; Yuan, X. Z.; Liu, G. Y.; Wei, B.; Zhang, Z.; Li, H.; Wang, H. J., A Review of Proton Exchange Membrane Water Electrolysis on Degradation Mechanisms and Mitigation Strategies. *J. Power Sources* **2017**, *366*, 33-55.

(71) Maljusch, A.; Conradi, O.; Hoch, S.; Blug, M.; Schuhmann, W., Advanced Evaluation of the Long-Term Stability of Oxygen Evolution Electrocatalysts. *Anal. Chem.* **2016**, *88*, 7597-7602.

(72) Oh, H. S.; Nong, H. N.; Reier, T.; Bergmann, A.; Gliech, M.; de Araujo, J. F.; Willinger, E.; Schlogl, R.; Teschner, D.; Strasser, P., Electrochemical Catalyst-Support Effects and Their Stabilizing Role for Iron Nanoparticle Catalysts During the Oxygen Evolution Reaction. *J. Am. Chem. Soc.* **2016**, *138*, 12552-12563.

(73) Reier, T.; Oezaslan, M.; Strasser, P., Electrocatalytic Oxygen Evolution Reaction (OER) on Ru, Ir, and Pt Catalysts: A Comparative Study of Nanoparticles and Bulk Materials. *ACS Catal.* **2012**, *2*, 1765-1772.

(74) Kim, Y. T.; Lopes, P. P.; Park, S. A.; Lee, A. Y.; Lim, J.; Lee, H.; Back, S.; Jung, Y.; Danilovic, N.; Stamenkovic, V.; Erlebacher, J.; Snyder, J.; Markovic, N. M., Balancing Activity, Stability and Conductivity of Nanoporous Core-Shell Iridium/Iridium Oxide Oxygen Evolution Catalysts. *Nat. Commun.* **2017**, *8*, 8.

(75) Zhu, Y. Q.; Cao, C. B.; Tao, S.; Chu, W. S.; Wu, Z. Y.; Li, Y. D., Ultrathin Nickel Hydroxide and Oxide Nanosheets: Synthesis, Characterizations and Excellent Supercapacitor Performances. *Sci. Rep.* **2014**, *4*, 5787.

(76) Godinez-Salomon, F.; Hallen-Lopez, M.; Solorza-Feria, O., Enhanced Electroactivity for the Oxygen Reduction on Ni@Pt Core-Shell Nanocatalysts. *Int. J. Hydrogen Energy* **2012**, *37*, 14902-14910.

(77) Garsany, Y.; Ge, J. J.; St-Pierre, J.; Rocheleau, R.; Swider-Lyons, K. E., Analytical Procedure for Accurate Comparison of Rotating Disk Electrode Results for the Oxygen Reduction Activity of Pt/C. *J. Electrochem. Soc.* **2014**, *161*, F628-F640.

(78) Kresse, G.; Furthmuller, J., Efficiency of Ab-Initio Total Energy Calculations for Metals and Semiconductors Using a Plane-Wave Basis Set. *Comput. Mater. Sci.* **1996**, *6*, 15-50.

(79) Kresse, G.; Hafner, J., Ab Initio Molecular Dynamics for Liquid Metals. *Phys. Rev. B* **1993**, *47*, 558-561.

(80) Kresse, G.; Hafner, J., Ab Initio Molecular-Dynamics Simulation of the Liquid-Metal Amorphous-Semiconductor Transition in Germanium. *Phys. Rev. B* **1994**, *49*, 14251-14269.

(81) Hammer, B.; Hansen, L. B.; Norskov, J. K., Improved Adsorption Energetics within Density-Functional Theory Using Revised Perdew-Burke-Ernzerhof Functionals. *Phys. Rev. B* **1999**, *59*, 7413-7421.

(82) Blochl, P. E., Projector Augmented-Wave Method. *Phys. Rev. B* **1994**, *50*, 17953-17979.

(83) Kresse, G.; Joubert, D., From Ultrasoft Pseudopotentials to the Projector Augmented-Wave Method. *Phys. Rev. B* **1999**, *59*, 1758-1775.

(84) Henkelman, G.; Uberuaga, B. P.; Jonsson, H., A Climbing Image Nudged Elastic Band Method for Finding Saddle Points and Minimum Energy Paths. *J. Chem. Phys.* **2000**, *113*, 9901-9904.

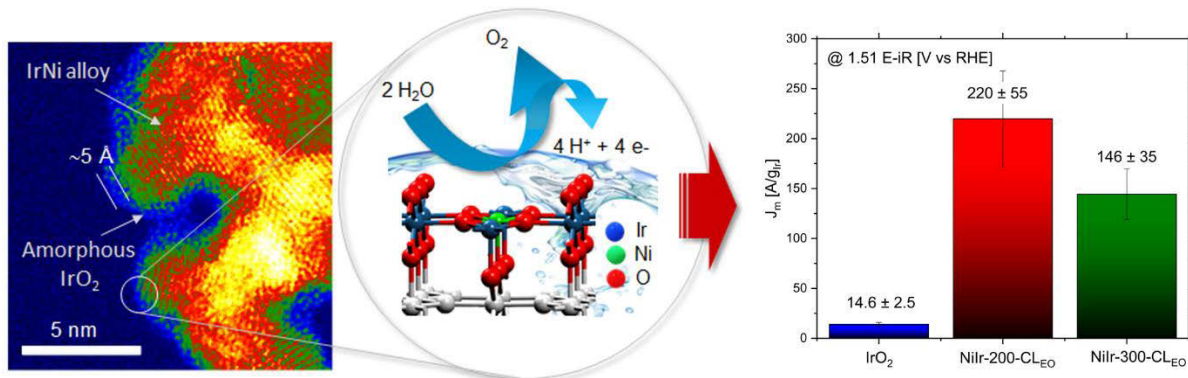
(85) Sheppard, D.; Terrell, R.; Henkelman, G., Optimization Methods for Finding Minimum Energy Paths. *J. Chem. Phys.* **2008**, *128*, 10.

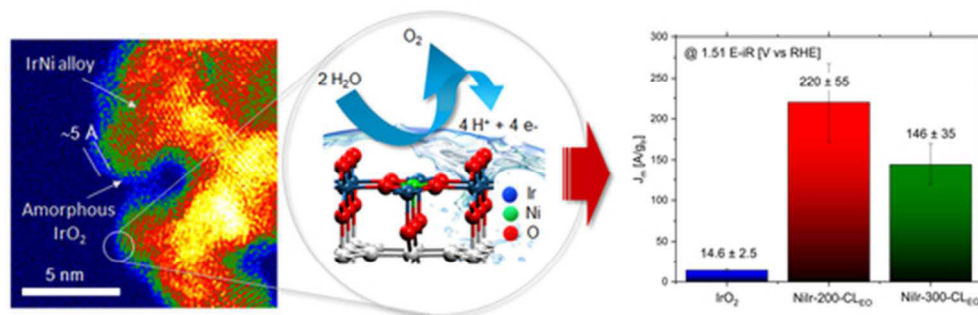
(86) Tang, W.; Sanville, E.; Henkelman, G., A Grid-Based Bader Analysis Algorithm without Lattice Bias. *J. Phys.-Condes. Matter* **2009**, *21*, 7.

1
2
3 (87) Sanville, E.; Kenny, S. D.; Smith, R.; Henkelman, G., Improved Grid-Based
4 Algorithm for Bader Charge Allocation. *J. Comput. Chem.* **2007**, *28*, 899-908.

5 (88) Henkelman, G.; Arnaldsson, A.; Jonsson, H., A Fast and Robust Algorithm for Bader
6 Decomposition of Charge Density. *Comput. Mater. Sci.* **2006**, *36*, 354-360.
7
8
9
10
11
12
13
14
15
16
17
18
19
20
21
22
23
24
25
26
27
28
29
30
31
32
33
34
35
36
37
38
39
40
41
42
43
44
45
46
47
48
49
50
51
52
53
54
55
56
57
58
59
60

Table of Contents Graphical Abstract





45x24mm (300 x 300 DPI)